Federal University of Espírito Santo - UFES

Technology Center

Graduate Program in Electrical Engineering

Welton Sthel Duque

Development of an ultrasonic hydrophone based on a fiber optic Michelson's interferometer to measure the volume of liquids

Vitória-ES

2022

Welton Sthel Duque

Development of an ultrasonic hydrophone based on a fiber optic Michelson's interferometer to measure the volume of liquids

Dissertation submitted to the Graduate Program in Electrical Engineering of the Technology Center of the Federal University of Espírito Santo, as a partial requirement for obtaining a master's degree in Electrical Engineering.

Federal University of Espirito Santo
Technological Center
Graduate Program in Electrical Engineering

Advisor: Prof. Dr. Anselmo Frizera Neto
Co-advisor: Prof. Dr. Camilo Arturo Rodríguez Díaz
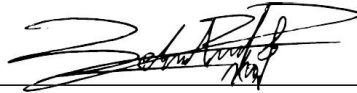
Vitória-ES

2022

Welton Sthel Duque

Development of an ultrasonic hydrophone based on a fiber optic Michelson's interferometer to measure the volume of liquids

Dissertation submitted to the Graduate Program in Electrical Engineering of the Technology Center of the Federal University of Espírito Santo, as a partial requirement for obtaining a master's degree in Electrical Engineering.

Dissertation approved. Vitória-ES, July 29th, 2022:

Prof. Dr. Anselmo Frizera Neto
(Advisor)

Prof. Dr. Camilo Arturo Rodríguez Díaz
(Co-advisor)

Prof. Dra. Maria José Pontes
(Federal University of Espírito Santo)

Prof. Dr. Carlos Alberto Ferreira Marques
(University of Aveiro, Portugal)

Vitória-ES

2022

To God, the Supreme Intelligence, and First Cause of all things.

To Jesus Christ, the highest moral perfection God has ever offered to humankind, as our best guide and model.

To Bruna, my love, my wife, my life, my person, my way, my everything; and to our Mateus, our beloved son, the best present we have been borrowed by God in this present life, to love, educate, guide, and make him a good, correct, just, and lovely person, as best as we can as parents.

To all scientists, professors, doctors, and masters of our country and world, who make from their research, art and love for the profession, the alignment between will and progress, a catalyst between knowledge, arduous work, accomplishment, and evolution.

Acknowledgements

Einstein: 'What I most admire about your art, is your universality. You don't say a word, yet the world understands you!'

Chaplin: 'True. But your glory is even greater! The whole world admires you, even though they don't understand a word of what you say.'

(Albert Einstein and Charlie Chaplin at 'City of Lights' premiere, in 1931)

Abstract

Sensing technologies with optical fibers have been studied and applied since the 1970s in oil and gas, industrial, medical, aerospace, and civil areas. Detecting ultrasound acoustic waves through fiber-optic hydrophones (FOH) sensors can be one solution for continuous measurement of volumes inside production tanks used by these industries. So, this work presents a FOH system composed of two optical fiber coils made with commercial SMF (Single Mode Fiber), working in the sensor head of a Michelson's interferometer (MI), supported by an active stabilization mechanism that drives other optical coil wound around a piezoelectric actuator (PZT) in the reference arm, to mitigate external mechanical and thermal noises come from the environment. A graduated cylinder glass of 1000 ml is used as a test tank filled with water, inside which the sensor head and an ultrasound source are placed at. As a means of detection, amplitudes and phases are measured, and machine learning algorithms predict their respective liquid volumes. The acoustic waves create patterns electronically detected with resolution of 1 ml, and sensitivity of 349 mrad/ml and 70 mvolts/ml. The non-linear behavior of both measurands required the analysis of classification, distance metrics and regression algorithms to define an adequate model. The results show the system can decide liquid volumes with the accuracy of 99.4% using a k-NN (k Nearest Neighbors) classification with one neighbor and Manhattan's distance. Moreover, a gaussian process regression using rational quadratic metrics presented and RMSE (Root Mean Squared Error) of 0.211 ml.

Keywords: liquid-volume measurements; fiber-optic hydrophone; Michelson's interferometer; ultrasound acoustics; active stabilization; machine learning.

Resumo

As tecnologias de sensoriamento por meio de fibras ópticas vêm sendo estudadas e aplicadas desde a década de 1970, nas áreas de petróleo e gás, industrial, médica, aeroespacial e civil. A detecção de ondas de ultrassom por meio de hidrofones ópticos pode ser uma solução para a medição contínua de volumes de líquidos dentro de tanques de produção utilizados por essas indústrias. Assim, este trabalho apresenta um hidrofone óptico composto por duas bobinas feitas com fibra óptica comercial, instaladas no braço sensor de um interferômetro de Michelson, apoiado por um mecanismo de estabilização ativa que aciona outra bobina óptica enrolada ao redor de um atuador piezoelétrico situado no braço de referência do interferômetro, para mitigar ruídos mecânicos e térmicos provenientes do ambiente externo. Uma proveta cilíndrica graduada com capacidade de 1000 ml é usada como tanque de teste contendo água, dentro do qual são colocadas as bobinas do braço sensor e uma fonte de ultrassom. Como meio de detecção, amplitudes e fases são medidas e algoritmos de aprendizado de máquina preveem os respectivos volumes de líquido. As ondas acústicas criam padrões estacionários dentro do tanque, que são detectados eletronicamente com resolução de 1 ml e sensibilidade de 349 mrad/ml e 70 mvolts/ml. O comportamento não linear das medições foi analisado com diferentes algoritmos de classificação, métricas de distância e algoritmos de regressão, para se definir um modelo. Os resultados mostram que o sistema pode decidir volumes de líquidos com acurácia de 99,4% por meio da classificação k-NN (k-vizinhos mais próximos) usando-se apenas um vizinho e distância de Manhattan. Além disso, a regressão de processo gaussiano apresentou raiz de erro quadrático médio de 0,211 ml.

Palavras-chave: medição de volume de líquidos; hidrofone óptico; interferômetro de Michelson; acústica de ultrassom; estabilização ativa; aprendizagem de máquina.

List of Figures

List of Tables

List of Acronyms

BS	Optical Beam Splitter
BW	Bandwidth
CAPEX	Capital Expenditure
CW	Continuous Sinusoidal Wave
EF	Electronic Feedback Loop Circuit
EMI	Electromagnetic Interference
FOH	Fiber-Optic Hydrophone
FPI	Fabry-Perrot Interferometer
FRM	Faraday Rotator Mirror
GPR	Gaussian Process Regression
IS	Optical Isolator
k-NN	k-Nearest Neighbor
K_p	Voltage-phase coefficient [rad/V]
K_d	Phase-voltage coefficient [V/rad]
MI	Michelson's Interferometer
MZI	Mach-Zehnder Interferometer
OC	Optical Circulator
OFS	Optical Fiber Sensors
OP	Oscilloscope
OPEX	Operational Expenditure
PC	Polarization Controller
PD	Photodetector
PVDF	Polyvinyledine Fluoride
PZT	Piezoelectric actuator
RMSE	Root Mean Squared Error
SMF	Single Mode Optical Fiber
SG	Signal Generator
TNL Laser	Teraxion Narrow Linewidth Laser
UT	Ultrasound Transducer
VDC	Volts of Direct Current

Contents

1   INTRODUCTION

1.1   MOTIVATION

Alexander Graham Bell published the first scientific work associating acoustic waves and light (BELL, 1880). Since then, tenths of years have passed, technologies have improved exponentially, and nowadays optical fibers have been worldwide used in long distances for ultra-high bit rates in telecommunication systems (FORESTIERI et al., 2021), but also for sensor applications (DÍAZ, Camilo A. R. et al., 2019), including sensing acoustic waves through light modulation (COLE, James H. et al., 2011), like somehow did Bell, in 1880.

The use of optical fibers as acoustic sensors was first demonstrated in 1977 (BUCARO; DARDY; CAROME, 1977a). Optical fibers sensors (OFSs) have been studied and applied for industries of petroleum exploration, fuel storage and transportation, industrial manufacturing, military, chemical processing, medical, aerospace, food, and civil engineering (CAMPANELLA et al., 2018; CULSHAW, 2017; YIN; RUFFIN; YU, 2008).

The oil and gas industries require control techniques for their vessels with the aim of increasing the production rates, avoiding environmental contaminations, mitigating the human labor risks, and reducing the costs of plant setup investments (CAPEX), operations, and maintenance (OPEX) (LEAL-JUNIOR et al., 2018). A problem in these industries is the need of continuous monitoring of liquid volumes inside separation vessels working under the presence of dynamic emulsion and foam layers, accumulation of unwanted solids, sand in the bottom and sludge on the walls, besides turbulences caused by fluids injections, corrosive substances, and explosive atmospheres (DA SILVA MARQUES et al., 2015; HJERTAKER, 2001).

Ultrasound-based sensors employ acoustic transmitters and receivers immersed in liquids to calculate the acoustic impedance between adjacent layers of fluids (HJERTAKER; JOHANSEN; JACKSON, 2001). At reception, piezoelectric hydrophones can be constructed with polymers, like polyvinyledine fluoride (PVDF), that enable them to provide an output voltage that varies according with the acoustic pressure incident on them (RUPITSCH, 2019). Besides the PVDF types, there are ultrasound sensors made with optical fibers (BUICK et al., 2004; CHANG; ZHU; YANG, 2015; DE PAULA; COLE; BUCARO, 1983; FAN et al., 2019; FAN; CHEN; BAO, 2020; MA et al., 2016; MENG et al., 2021; MORRIS et al., 2006; WURSTER; STAUDENRAUS; EISENMENGER, 1994; YANG, Y. et al., 2021).

Compared to other sensing technologies, optical fiber sensors (OFSs) offer advantages as they are electrically (galvanic) isolated, immune to electromagnetic interferences (EMI), intrinsically safe, resistant to chemical corrosion, workable at elevated temperatures, wide bandwidth, capable of multiplexing, min-

imally invasive, they have good accuracy and resolution, reduced sizes and weights, their interrogator systems can be installed far from the remote monitored points, and they do not require any electrical power at the measuring points (DÍAZ, Camilo Arturo Rodríguez et al., 2018; LEAL-JUNIOR et al., 2018; VORATHIN et al., 2020). The OFSs are precise in measuring pressure, temperature, acoustic fields, strain, torsion, deformation, curvature, force, vibration, acceleration, rotation, humidity, viscosity and chemical parameters (DÍAZ, Camilo Arturo Rodríguez et al., 2019; WILD; HINCKLEY, 2008; YANG, F. et al., 2019; YIN; RUFFIN; YU, 2008).

In 1977, it was first demonstrated by (BUCARO; DARDY; CAROME, 1977a) the possibility of a direct acousto-optic interaction between an ultrasound field and an optical fiber coil working as an acoustic sensor. The acousto-optic effect is based on the physics principle that a propagating acoustic wave modifies the refractive index of a fluid through pressures variations and densities (BUICK et al., 2004), as a function of time and space. An experiment using a laser beam crossing a tank of water under ultrasonic waves ranging from 0.1 Hz to 180 kHz and a pressure $\Delta p = 18\,kPa$ resulted in a change of $\delta = 0.146\,\mu m$ in the optical path length, showing an magnitude order of $10^{-6}\,m$ (BUICK et al., 2004).

The authors of (BUCARO; DARDY; CAROME, 1977a) used 4 meters of a SMF optical fiber section length to build a coil of 10 turns and 3.3 cm diameter, and submerged it into water so that its optical beam was phase modulated by ultrasound waves ranging from 40 to 400 kHz. The optical fiber coil sensitivity was characterized by the light phase shifts whose intensity depended upon the acoustic pressure incident on the optical fiber length, with which a MI has been employed (COLE, J. H.; JOHNSON; BHUTA, 1977; MASSEY, 1968; MOSS; MILLER; FORWARD, 1971).

Fiber-optic hydrophone (FOH) is an acoustic sensor that uses optical fibers as the sensing element, which can be applied in fields such as oil and gas exploration, earthquakes inspection and underwater objects detection (HU; LI; LIU, 2017; MENG et al., 2021). An usual scheme applied with FOH are those based on optical interferometry, which offer greater sensitivities than the piezoelectric hydrophones, and they pertain to the class of phase-modulated sensors (KROHN; MACDOUGALL; MENDEZ, 2014; LEE et al., 2012; YIN; RUFFIN; YU, 2008). An FOH system measures the light phase changes induced by a particular measurand (YIN; RUFFIN; YU, 2008), in which an ultrasound piezoelectric source (UT) works as a transmitter and an optical fiber sensor works as the receiver (HJERTAKER; JOHANSEN; JACKSON, 2001; MERIBOUT; NAAMANY; BUSAIDI, 2009).

Interferometric schemes can be mounted by using commercial available optical components (LIANG et al., 2016). Four interferometers configurations are usually cited by the literature: Fabry-Perot, Mach-Zehnder, Michelson's, and Sagnac, as they provide good sensitivities, accuracies, large dynamic ranges, and may cover long distances of monitored points (LEE et al., 2012). The latter three types are also known as two-beam interferometers (WATCHI et al., 2018).

1.2 PROBLEM AND JUSTIFICATION

Publications about FOHs have demonstrated their work principles, showing them as an alternative technology to replace the piezoelectric hydrophones (STAUDENRAUS; EISENMENGER, 1993). FOHs do not need recalibration (SHEN et al., 2011) and present higher bandwidths than the conventional piezoelectric hydrophones (SHAO et al., 2008). Interferometric techniques can be used to improve their sensitivities (HU; LI, 2016), resolutions, bandwidths, dynamic ranges, signal to noises ratios (KIRKENDALL; DANDRIDGE, 2004). A twisted pair made with single-mode fibers has been recently published as a high-sensitivity broadband ultrasound sensor able to work from 20 kHz to 94.4 MHz (FAN et al., 2020). These publications are focused on the technology aspects of the FOH.

Other papers present applications and proof of concepts with the use of FOH sensors. As examples, the largest array of FOHs in the world is composed by 16000 sensor elements, as a commercial solution used undersea to permanent monitor oil reservoirs in the North Sea (MENG et al., 2021). A FOH is used to precisely detect cavitation bubbles under high ultrasound emissions (KIMURA; TAKEUCHI; KOIKE, 2020). Two line arrays each composed by 32 elements were deployed off the San Diego's cost for object recognition underseas (DAVIS et al., 2015). A FOH was used to measure the power of hyperthermia transducers without being damaged (CHAN et al., 1989). And, a 50 MHz wideband FOH was developed to measure medical ultrasound fields (MORRIS; BEARD; HURRELL, 2005).

To the best of our knowledge, it was challenging to find out published works describing laboratory prototypes of a FOH system to measure liquid volumes and presenting results of accuracies and RMSE derived from machine learning algorithms. There are publications describing the behavior of underwater optical coils, but they do not present results of using these coils to measure liquid volumes (AL-NAAMANY; MERIBOUT; AL BUSAIDI, 2007; BEARD; HURRELL; MILLS, 2000; CHANG; ZHU; YANG, 2015; MA et al., 2016; WANG, M. et al., 2018; WANG, W. et al., 2020; WURSTER; STAUDENRAUS; EISENMENGER, 1994; YANG, Y. et al., 2021). Ultrasound methods to determine multilayers of oil, emulsion, and water in oil tanks are demonstrated in (AL-NAAMANY; MERIBOUT; AL BUSAIDI, 2007; FAISAL; BUKHARI; YANG, 2006; HJERTAKER, 2001), and show the advantages of FOH, like contactless distance measurement, low cost, high precision, simple setup, independence of intensity of dusty and smoky environment. However, there were not results regarding to liquid volume measurements.

1.3 OBJECTIVES

Considering a FOH system as a new generation (MENG et al., 2021) and a primary application (KIRKENDALL; DANDRIDGE, 2004) for underwater acoustic sensor, and underwater detection (YANG, Y. et al., 2021), the objective of this work is to present a prototype composed by optical fiber coils in the MI's

sensor head, with an active stabilization mechanism driving other optical coil wound around a piezoelectric actuator in the MI's reference arm, and a software application that uses amplitudes and phases of detected acoustic signals to predict the liquid volumes by means of machine learning algorithms.

The specific objectives were defined as follows:

a) To propose an optical hydrophone model based on the interferometry technique, with which the final sensor will be experimentally evaluated and proved suitable for detection of fluids.

b) To characterize the hydrophone in terms of its characteristics and acoustic performance, bandwidth in hertz, and sensitivity.

c) To evaluate and present different machine learning algorithms, both classification and regression types, and their results of accuracy and root mean squared error, respectively.

Although the isolated functions of the purposed system have been already studied and applied in known applications, the novelty of this proposal is the fact of bringing together those functions, like: underwater acoustic waves detection; optical coils as sensing elements; an optical interferometry scheme; an electronic circuit for homodyne detection and active stabilization of noises; other optical coil wound around a piezoelectric actuator; the use of electric phase differences between the acoustic signals inputted and outputted by the sensor; and the definition, testing and comparison of several data models processed by machine learning algorithms, offering new insights and results with high accuracies and low errors for an application of liquid volume measurement.

1.4   DISSERTATION STRUCTURE

In section 1, this dissertation presents an introduction about fiber-optic sensors, hydrophones, and related applications. Section 2 presents a theoretical background acoustics detection and section 3 describes the material and methods employed on the experiment setup. Then, section 4 presents the results and discussions. Finally, section 5 ends the paper with conclusions and future works suggestions.

2   THEORETICAL BACKGROUND

The MI has been chosen to this work due to its simple configuration, the need of fewer fiber splices and one beam splitter (KIRKENDALL; DANDRIDGE, 2004; LEE et al., 2012). Besides, it accepts flexible geometries and has lower component costs, compared to other schemes (WANG, C. C. et al., 1994; YIN; RUFFIN; YU, 2008). These characteristics were taken into consideration to choose the MI as the sensor head of this work.

2.1   MICHELSON'S INTERFEROMETER

A MI, whose picture is adapted from (YIN; RUFFIN; YU, 2008) (p. 371), is presented in Figure 1, in which a 3 dB beam splitter (BS) divides the power of an input coherent laser (KROHN; MACDOUGALL; MENDEZ, 2014) between two arms defined as optical paths, which are ended by mirrors that reflect the optical beams back. The optical paths can be a free-space air, or tubes with gases, or vacuum, or optical fibers. The two optical beams are then reflected back by the MI arms and optically recombined at the BS after which a photodetector converts this combined optical signal to an electronic voltage value that represents the phase changes differences among both interferometer arms.

Considering an MI fed with the power P_{IN}, the light wavelength in the medium λ, a wave number $k = 2\pi/\lambda$, and a lossless beam splitter with a division rate of 0.5, the relation between the output power P_{OUT} and the interferometer's optical path differences $\Delta L = L_S - L_R$ can be expressed by (WATCHI et al., 2018):

$$P_{OUT} = \frac{P_{IN}}{2}\left[1 + \cos\left(\frac{4\pi\Delta L}{\lambda}\right)\right] \tag{1}$$

The first MI arm is called the 'sensor head' or 'wet arm', it has a length L_S and is exposed to measurands, like sound, pressure, temperature, strain, and mechanical vibrations. The other arm is known as the 'reference arm' or 'dry arm', it has a length L_R and should be isolated from environment disturbances (YIN; RUFFIN; YU, 2008).

A desired measurand induces changes on the sensor head that dynamically changes its physical fiber length L_S, leading to a path difference ΔL among the two arms, that induces phase differences $\Delta \phi$ between their light beams, resulting in phase changes that are electronically expressed by a photodetector (YIN; RUFFIN; YU, 2008).
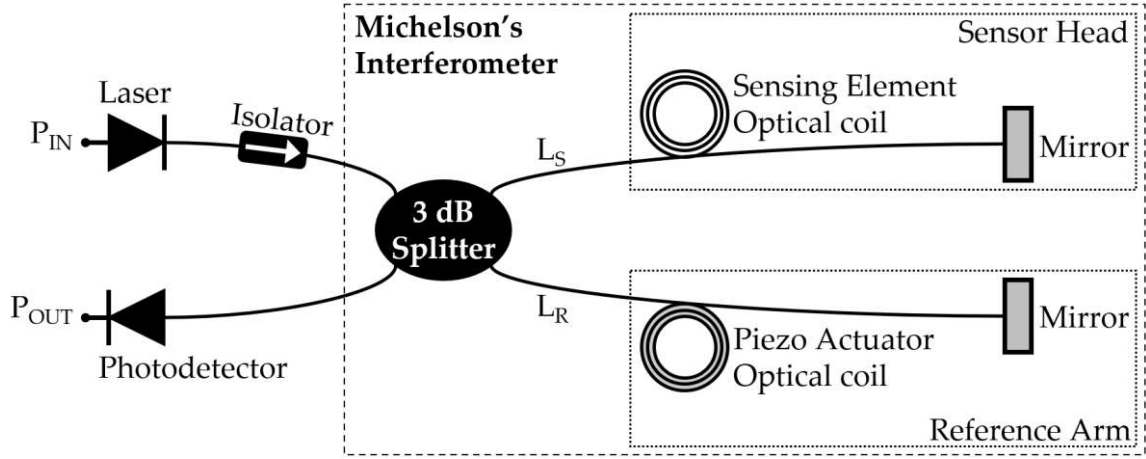
Figure 1. A FOH based on a Michelson's interferometer.

A linear polarization of a light beam in one MI arm can be expressed by (KROHN; MACDOUGALL; MENDEZ, 2014):

$$\vec{E}(z, t) = E_0 \cos\left[\omega_0 t - \left(\frac{2\pi}{\lambda}\right) z\right], \tag{2}$$

where $\vec{E}$ is the electrical field of the optical electromagnetic wave, E_0 is its maximum amplitude, ω_0 is the optical wave frequency in radians per seconds, z is the longitudinal space point, and t is the time.

Equation (2) shows amplitudes that might be present on the transverse $\vec{x}$ or on the $\vec{y}$ space coordinates, propagating through the longitudinal $\vec{z}$ coordinate. Considering the fiber physical length L, the light speed in vacuum c_0, the vacuum wavelength λ_0, the fiber refraction index n, the wave group velocity $v = c_0/n$, what leads to $1/\lambda = n/\lambda_0$, the electrical field can be expressed by:

$$\vec{E} = E_0 \cos\left[\omega_0 t - \left(\frac{2\pi n}{\lambda_0}\right) L\right], \tag{3}$$

and the Equation (4) shows the fixed phase angle ϕ_0 (in radians) of the light beam. The term $'nL'$ is defined as the 'optical path length' (UDD; WILLIAM B. SPILLMAN, 2011).

$$\phi_0 = \frac{2\pi n L}{\lambda_0}, \tag{4}$$

and changes in L or n lead to the phase variations expressed by:

$$\phi_0 + \Delta\phi = \frac{2\pi}{\lambda_0} [n.L + n.\Delta L + \Delta n.L], \tag{5}$$

where $\Delta\phi$ are the incremental phase changes due to incremental length changes ΔL, which induce refractive index variations Δn due to the optical fiber photo-elastic effect. Also, frequency variations (jitter) from the laser source may also contribute to phase drifts, and the Equation (5) can be expressed as a sum of derivatives of the terms involved in the phase drifts (UDD; WILLIAM B. SPILLMAN, 2011):

$$\frac{d\phi}{\phi} = \frac{dL}{L} + \frac{dn}{n} + \frac{dk}{k} \tag{6}$$

Current optical detection systems estimate the average power per unit area and unit time as a measure of intensity or irradiance I_{OUT}, which is proportional to the squared amplitude of the electrical field (REIDER, 2016):

$$I_{OUT} \approx E_0{}^2 \tag{7}$$

The summation of both arms light waves ($\vec{E}_T = \vec{E}_R + \vec{E}_s$) results in an irradiance perceived by the photodetector (KROHN; MACDOUGALL; MENDEZ, 2014), that can be expressed by:

$$I_{OUT} = 2E_0{}^2[1 + \cos(\Delta\phi)], \tag{8}$$

where $\Delta\phi = \phi_R - \phi_S$ is the phase difference of both light waves summation.

In another view, this phase difference can also be represented by $\Delta\phi = \phi_e - d\phi_m$, in which ϕ_e is the bias phase standing for the external disturbances with low frequency and slow drifts with time, affecting both interferometer arms (sensor and reference). The second term $d\phi_m$ represents the pure physical measurand variations of interest whose value represents the interferometer's sensor arm (KIRKENDALL; DANDRIDGE, 2004).

When the interferometer is forced to keep its bias phase ϕ_e around the $(2n + 1) * \pi/2$ radians points, it reaches a condition called quadrature state, in which it supplies a better response to the measurand $d\phi_m$. The nature of sinusoidal waves at the quadrature point limits the two-beam interferometers to work under the largest optical phase displacements of half a wavelength. And, when the bias phase ϕ_e is located around zero or on multiple integers of $\pm\pi$ radians, the resulting interferometric pattern jumps between zero and maximum peak values, representing the worst sensitivity points, as the derivatives of intensity to phase are zero at them (GRASSANI; GALLI; BAJONI, 2014; KIRKENDALL; DANDRIDGE, 2004; KROHN; MACDOUGALL; MENDEZ, 2014; WATCHI et al., 2018).

Although $\Delta\phi$ may appear to be a stable measurand, the noises present on ϕ_e can be so elevated that the measurand $d\phi_M$ may become impossible to be read (KIRKENDALL; DANDRIDGE, 2004; KROHN; MACDOUGALL; MENDEZ, 2014). More details about the MI working as an optical hydrophone for signal intensity (irradiance) and phase (homodyne or heterodyne) measurands detection can be obtained from other studies: (CHANG; ZHU; YANG, 2015; ELEZOV et al., 2018; GRASSANI; GALLI; BAJONI, 2014; KIRKENDALL; DANDRIDGE, 2004; KROHN; MACDOUGALL; MENDEZ, 2014; LEE et al., 2012; MENG et al., 2021; UDD; WILLIAM B. SPILLMAN, 2011; WILD; HINCKLEY, 2008; XIE; CHEN; REN, 2009; YANG, Y. et al., 2021; YIN; RUFFIN; YU, 2008).

2.2 MICHELSON'S INTERFEROMETER FOR ACOUSTIC WAVES DETECTION

Taking into consideration the equations and terms already presented, a MI whose sensor arm is composed by a single-mode optical fiber coil immersed in a liquid, within which propagates an acoustic field of pressure P_a and angular frequency ω_a, the interferometer's resulting light beam is expressed by (BUCARO; DARDY; CAROME, 1977a):

$$\vec{E} = E_0 \exp i(\omega_0 t) + E_0 \exp i(\omega_0 t + K_a \sin(\omega_a t) + \Delta\phi), \tag{9}$$

where K_a is the modulation index that defines the acoustic influence on the phase drifts, and $\Delta\phi$ is the dynamic optical phase differences between both MI arms. For a uniform acoustic field, K_a is expressed below, and L_c is the physical length of the optical fiber coil interacting with the acoustic wave (BUCARO; DARDY; CAROME, 1977a):

$$K_a = \frac{2\pi}{\lambda_0} \frac{\partial n}{\partial P_a} P_a n L_c \tag{10}$$

Bucaro *et al.* (BUCARO; DARDY; CAROME, 1977a) also defines S_d as constant that defines the detector's sensitivity, which depends on the photodetector's gain G, quantum efficiency q, electron charge $e = 1.602 * 10^{-19}$ [c], on the Planck's constant $h = 6.626 * 10^{-34}$ [m^2 kg/s], and on other terms already presented, as expressed by:

$$S_d = \frac{2\pi Gqe}{hc_0 k} \tag{11}$$

Finally, it is shown by (BUCARO; DARDY; CAROME, 1977b, a) that small values of modulation index K_a will result in the following irradiance equation perceived by the MI hydrophone:

$$I_{OUT} = 4E_0{}^2 S_d \left[1 + \cos(\Delta\phi) - \frac{K_a}{2} \sin(\Delta\phi) \sin(\omega_a t) \right] \tag{12}$$

2.3 ACTIVE STABILIZATION FOR HOMODYNE DETECTION

The phase instabilities inherent to optical interferometers represent a challenge that requires counter measures to mitigate the problem (WATCHI et al., 2018). In an ideal scenario, the MI works properly when its arms are equal in length (balanced condition), and the reference arm is isolated from external noises (CHANG; ZHU; YANG, 2015; ELEZOV et al., 2018; GRASSANI; GALLI; BAJONI, 2014; XIE; CHEN; REN, 2009). So, these noises on the MI measurements are needed to be controlled by adjustment mechanisms [6–8], like Pockels cell (PRESTON et al., 1999), rubbers and springs for anti-vibrations (MOSS; MILLER; FORWARD, 1971), optical tables, hermetic boxes and thermal bath (ELEZOV et al., 2018), piezoelectric actuators (CHANG; ZHU; YANG, 2015; XIE; CHEN; REN, 2009), sensing information encoded in a carrier signal, phase generated carrier, and active homodyne demodulation (KIRKENDALL; DANDRIDGE, 2004). Despite

the fact the solutions aim to achieve the MI's stabilization, not always they are continuously stable in time, and, as reported by (MOSS; MILLER; FORWARD, 1971), sometimes actions of noise isolation 'are still an art rather than a science'.

2.4 CONCEPTS OF MACHINE LEARNING

This section introduces basic concepts about machine learning and the respective algorithms used in this work, without getting too deep in the theories of this wide thematic area. There is a plenty of books and papers related to this knowledge which can be consulted by the reader for more details. The following sections present some of these references used in this work, according to the context and defined applications.

From the seventieth decade and until now, the complexity of problems and volumes of data increased in several knowledge areas, challenging the computing systems and their software to process and create results with speed and reliability. In this context, techniques based on artificial intelligence started to be applied by specialist and knowledge-based systems, to solve real world problems. The aim of turning these systems more autonomous, independent of human interventions, and able to induce new hypotheses and create new learning from past experiences, it all defines the concept of machine learning (KATTI FACELI, ANA CAROLINA LORENA, JOÃO GAMA, 2011), to which an intelligent behavior essentially depends on learning abilities and algorithms that improve with experience (MITCHELL, 1997).

2.4.1 Machine Learning Applications

Nowadays, machine learning has been widely used in several knowledge and scientific areas, like proving physics and mathematical theorems, universe events detection in astronomy, natural language processing, genetic sequencing analyses in biology, robotics and optics in electronic engineering, driving a car autonomously, playing chess like a Kasparov, diagnosing diseases, risks and futures predictions in finances, human behaviors detection, computer security, software engineering, computer vision and imaging processing, among others (CEJA, 2022; RUSSEL; NOVIG, 2022). This dissertation uses machine learning to prove the results of the math and physics model inherent to an optical sensor system.

Machine learning methods rely on three building blocks: data, algorithms, and models; in that every machine learning algorithm needs data to learn a model. The learning processes is known as the training phase using a training dataset, so a learned model can be used further to predict results from an aleatory, unknown, and new upcoming data of real-world applications, called production dataset, to be evaluated and categorized. Since the performance of the trained model needs to be evaluated before putting the algorithms into production, a test phase is performed with a test dataset, which is a set of data that have never been used for training purposes before. Finally, when the test dataset proves the trained model has

reached a minimum accuracy and performance, so the algorithm is ready to be used with production da-
taset to predict results from real-word applications (CEJA, 2022).

2.4.2   Objects and Features

In terms of data structure, a dataset is composed by rows and columns of data, like a two dimen-
sions matrix. In a simple view, a three dimensions data structure can also be represented as a two dimen-
sions matrix or data table, in which a new column of data is added do the table to represent the values of
third dimension. Indeed, a two-dimensional table represents a data structure of N dimensions, in which
each column is a dimension or feature, and each row is an object. In literature, one object row of this table
can be also referred as a data point, an instance, a tuple, a sample, or an observation. A feature column
can also be referred as a variable, an attribute, a dimension, or a property. Each feature can be seen as an
orthogonal axe (dimension) among all other features, defining a space, and each object is a point in this
space.

2.4.3   Classification and Regression

Usually, one of the features represents a category or a numeric result that can be represented by all
other features of the table. When this feature is a discrete or nominal category, like a specific color name,
a fruit type, a disease name, or an animal species name, the categorization type of algorithms are used.
However, when this feature is a continuous numerical value, like the numerical result of the independent
variables of a polynomial equation of N-order composed by N dependent variables, or the liquid tempera-
ture inside an oil production vessel, or the future price of a stock exchange, the regression type algorithms
are used (CEJA, 2022; KATTI FACELI, ANA CAROLINA LORENA, JOÃO GAMA, 2011; RUSSEL; NOVIG, 2022).

2.4.4   Supervised and Unsupervised Learning

Machine learning methods can be positioned among two extremes: supervised learning and unsu-
pervised learning. There are intermediate types among them that mix both supervised and unsupervised
characteristics. In supervised learning, both training and test datasets have predefined and known labels
or values registered in a specific feature of the table. In this case, the certainties of these labels or values
are 100% guaranteed, and all other features are just columns of data used to predict these labels (by cate-
gorization) or values (by regression). A production dataset does not have this predefined specific feature,
but a machine learning model is trained and used just to predict values for this feature, as a labeled cate-
gory or a regressed value. On the other hand, the unsupervised learning is an extreme case in which none
of the training or test datasets have a predefined label or known value to represent an object, and the
algorithm tries to automatically group different objects into meaningful clusters. Examples of clustering

methods are k-means, k-medoids, and hierarchical clustering. Besides clustering methods, there are other unsupervised ones, like association rules, word embeddings, and autoencoders (RUSSEL; NOVIG, 2022).

Examples of classification algorithms are Rocchio (Nearest Centroid), k-Nearest Neighbors (k-NN), decision trees, and Random Forest. And examples of regression models are gaussian process regression, linear regression, regression trees, and neural networks. There are cases in which the same algorithm can be used for both classification and regression purposes (CEJA, 2022).

After data are collected in raw state, they need to be explored, cleaned, and pre-processed, before submitted to a training and test phases of a machine learning algorithm. These steps involve actions of summarizing data; removing noises, outliers, and missing values; treating class imbalances; and normalization or standardization of features, scales, and ranges. When huge scales differences exist between two features of the same dataset, like a feature values ranging from 0.1 to 10, and other from 500 to 1000, it may severely affect the results of distance-based algorithms, like Rocchio and k-NN, and a normalization or standardization operation is needed to be applied on the data, before using it for training, test or prediction purposes (RUSSEL; NOVIG, 2022).

2.4.5 Standardizing or Normalizing Data

The normalizing operation scales a feature to a new range of values between 0 and 1, by using its maximum and minimum observed values. A feature can also be scaled to a range of fixed values, when there is previous and certain knowledge about the numerical nature of the feature. Supposing a vector of values x, ranging from $\min(x)$ to $\max(x)$, a specific value x_i can be normalized to a new value $\hat{x}_i$, that is, scaled to a new value between 0 and 1, through the following operation. In this case, $\min(x)$ and $\max(x)$ can also be replaced by predefined known and fixe values, that can be assumed by an object, although they are not present in the dataset (CEJA, 2022).

$$\hat{x}_i = \frac{x_i - \min(x)}{\max(x) - \min(x)} \tag{13}$$

The standardizing operation in equation below scales the values of a feature so that they assume a new distribution with zero mean and variance one (Z-score), in which μ is the mean and σ is the standard deviation of all collected values for the feature x, registered in a dataset (CEJA, 2022):

$$\hat{x}_i = \frac{x_i - \mu}{\sigma} \tag{14}$$

The choice between normalization or standardization will depend on the nature of the variables and on the preliminary analyses performed on the raw collected data, and the constraints and benefits of each method can be searched on the literature.

2.4.6 Distance Metrics used with Clustering

The hypothesis behind distance-based classifiers is that similar objects tend to stay closed to each other in the same region of a multidimensional space, grouped within a cluster. In the same meaning, non-similar objects would stay far from each other in this space. A cluster is an aggregation of objects in which the distance between any two objects of the same cluster is less than the distance between any two objects pertaining to different clusters, as seen in Figure 2. The main input to clustering algorithms, like Rocchio and k-NN used in this work, is the distance between all objects from each other (KATTI FACELI, ANA CAROLINA LORENA, JOÃO GAMA, 2011; MANNING; RAGHAVAN; SCHUTZE, 2008; XU et al., 2009).
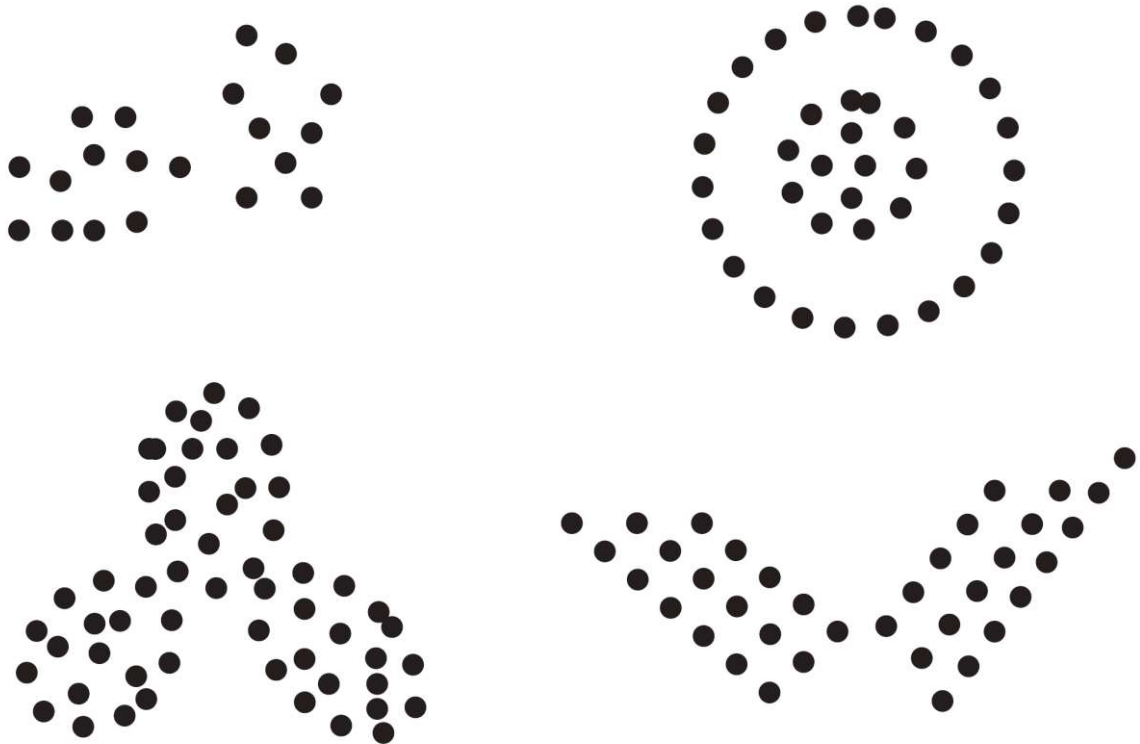
Figure 2. Examples of objects distributed in clusters on a two-dimensional space, in which four major clusters are seen on a coarse level, and nine minor clusters can be seen in a finer distribution (XU et al., 2009).

Clustering algorithms distribute data objects into different clusters according to the algorithm's technique itself and also according to the specific distance metrics used by the algorithm. The same algorithm can use different distance metrics and the same distance metric can be used by different algorithms. In this sense, this work has analyzed the results of two algorithms (Rocchio and k-NN) in which each one has been tested with the five different distance metrics described in Table 1 (XU et al., 2009).

Despite the fact that all distance metrics can calculate distances for objects with any number of features, as a matter of simplification, the formulae presented in the table below consider the distance $D(A, B)$ between two objects named A and B, of only two features each, named x and y. So, the values A_x, A_y, B_x and B_y are distinct numerical values for the features of both objects.

Table 1. Equations of distance metrics among two objects in a two-dimensional space.

Distance Metrics Names	Distance Equation
Euclidean	$D_{EUC}(A, B) = \sqrt{(A_x - B_x)^2 + (A_y - B_y)^2}$
Manhattan	$D_{MAN}(A, B) = |A_x - B_x| + |A_y - B_y|$
Mahalanobis	$D_{MAH}(A, B) = (A - B)^T * S^{-1} * (A - B)$
Cosine Similarity	$D_{SCO}(A, B) = \cos(A, B) = \dfrac{(A_x * B_x) + (A_y * B_y)}{\sqrt{A_x{}^2 + A_y{}^2} * \sqrt{B_x{}^2 + B_y{}^2}}$
Cosine Distance	$D_{DCO}(A, B) = 1 - D_{SCO}(A, B)$

From the Table 1 above, the Euclidean is the most commonly used distance measured and it creates hyperspherical clusters invariant to translations or rotations in the dimensional space. The Manhattan distance is known as the 'city-block' distance and it requires the less computational efforts compared to the other distance metrics, as it performs only addition and subtraction operations, while other distances use potentiation, square-root and matricial operations. The Mahalanobis tends to form hyperellipsoidal clusters, and the calculus of its distances involves matrix operations in which $(A - B)^T$ is the transpose operation of a vector containing the difference values of each feature, and S^{-1} is the inverse of the within-class covariance matrix. The Cosine Similarity is the normalized inner product of a pair of data objects as if they were vectors in space, in which the more similar the two objects, the more parallel their vectors are, and, therefore, the greater the cosine value of the angle among them. The Cosine Distance is the complement to one of the Cosine Similarity (XU et al., 2009).

Each clustering algorithm can always produce clusters for a given dataset, whether or not there really exists particular structures in the data. Besides, different algorithms, and even the selection of distinctive features for the same algorithm, can result in different clusters formations for the same data. Therefore, the effective evaluation of standards and criteria are critically important to provide confidence for the clustering results, in that the assessments should have no preferences to any algorithm, and should be able to provide meaningful insights in answering questions like how many clusters are hidden in the data, whether the clusters are meaningful from a practical point of view, or why we choose one algorithm instead of another (XU et al., 2009).

2.4.7 Rocchio and k-NN algorithms

The Rocchio method is a way to classify a new object by calculating its distance to the center to all different clusters present in the trained dataset, and label it with the closest cluster. The center of a cluster represents the mean values of all features, of all objects, which compound the trained dataset, so that a trained model is composed by n centroids (prototypes), where n is the number of different classes. This classifier calculates the centroid of each labeled class and has no parameters to optimize. The boundary between two classes in Rocchio classification is the set of points with equal distances from two or more centroids. The complexity of this technique is independent of the number of training samples, being only a function of the number of classes and number of attributes of the classification problem (CEJA, 2022; MANNING; RAGHAVAN; SCHUTZE, 2008).

The k-NN (k-Nearest Neighbor) algorithm is a simple yet robust categorization approach, that works surprisingly well on many problems, calculating the distances between one testing object to all labeled objects present in a trained dataset, from which it chooses the most frequent class among the k-nearest objects, and labels the tested object with that class (ALBALATE; MINKER, 2011; JAMES et al., 2021). The k-NN does not perform any centroid calculation like does the Rocchio's. It memorizes all objects of the trained dataset and then compares all of them with the new object being classified. For this reason, k-NN is also known as a lazy learning or memory-based learning algorithm. Although it is usually desirable to have as much training data as possible in the model, large training sets may cause severe efficiency problems in k-NN classification. (MANNING; RAGHAVAN; SCHUTZE, 2008).

A special case of k-NN is the 1-NN (only one nearest neighbor) version that defines the Voronoi tessellation in that each trained object defines a Voronoi cell. A two-dimensional Voronoi tessellation divides a plane into d convex polygons, in which d is the number of objects in the trained database. More dimensions divide a space in hyper-polygons. As a demonstrating example, Figure 3 shows a two-dimension plane with many objects classified and clustered in three classes: 'x', 'circle', and 'diamond'. The new and still unclassified object 'black star' will be classified as a 'circle' when 1-NN is used, as it falls into the Voronoi cell of a 'circle' object. However, if 3-NN were used in this example, the new object would be classified as an 'x', as the most frequent class among the three nearest neighbors is the 'x', even though a 'circle' object is still the closest one. And, finally, it would be classified as a 'circle' by the 7-NN classification. These examples show the importance of choosing the right value for 'k' to which it is recommended to always use small and odd values (KATTI FACELI, ANA CAROLINA LORENA, JOÃO GAMA, 2011; MANNING; RAGHAVAN; SCHUTZE, 2008).
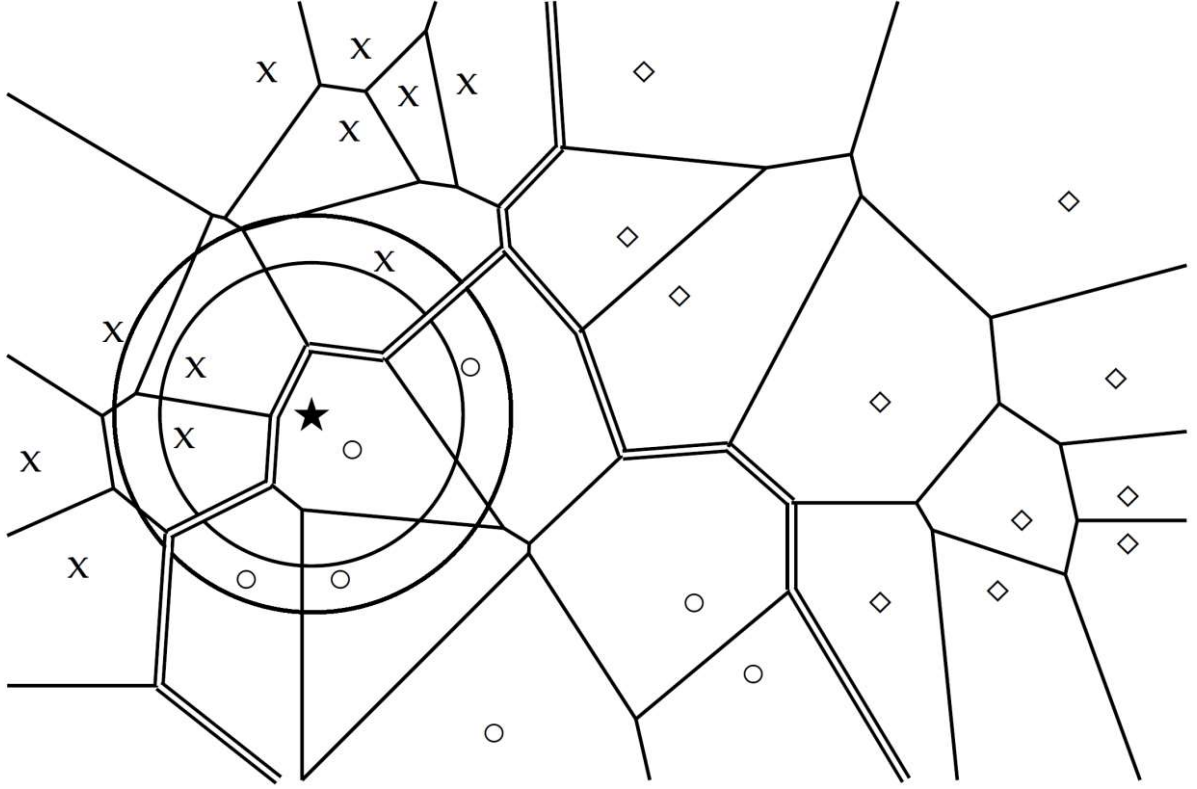
Figure 3. Voronoi tessellation and three classes where single lines are decision boundaries for 1-NN classification, and double lines are boundaries for the three trained object classes (MANNING; RAGHAVAN; SCHUTZE, 2008).

2.4.8   Gaussian Process Regression

The Gaussian Processes models are popular in machine learning applications due to their high flexibility. The Gaussian Process Regression (GPR) technique assumes that the dependent variable of a linear regression assumes a gaussian distribution, so that, instead choosing a specific parametric distribution to form the regression function, it is chosen the mean vector and the covariance matrix derived from the data model attributes, to predict a fitting model (ROGERS; GIROLAMI, 2017).

A desired and continuous fitting function $f(x)$ based on a training dataset is obtained so to make predictions of new and unseen values for and inputted value of x. The central assumption made by GPR is that a collection of continuous outputs for $f(x)$ are sampled to a vector f_n, and associated to a sampled input vector x_n, in which f_n and x_n are assumed to be jointly Gaussian distributed. Although there are infinite values for x what would imply to an infinite-dimensional vector f_n, a key property of a multivariate gaussian density is that any subset of the f_n elements also are multivariate gaussian with mean values and covariance matrix simply extracted from the training dataset. Therefore, it is not necessary to know all possible values of x, but only the ones present in the training and test datasets, considering a popular choice for the mean function as $\mu(x_n) = 0$, and an RBF (radial basis function) stationary covariance matrix, which performs very well in a wide range of applications (ROGERS; GIROLAMI, 2017).

3   MATERIALS AND METHODS

This FOH system is based on physics principles of acoustic waves reflecting in liquids in that the acoustic path is changed by changes on the volume of water (AL-NAAMANY; MERIBOUT; AL BUSAIDI, 2007).

3.1   EXPERIMENTAL SETUP

The experiment setup in Figure 4 shows a FOH system for liquid volume measurement, based on the MI, with an electronic feedback (EF) loop circuit to compensate external noises from the sensor's measurands. The system outputs a sinusoidal signal from which two values are extracted: amplitude and phase. The phase is the difference between the acoustic field delivered to the UT, and the acoustic field detected by two optical coils S1 and S2, placed at the sensor head. For each differential volume of water added to or extracted from the tank, the length of the water (acoustic path) changes and the internal water surface dislocates. Thus, a new profile of internal sound backscattering inside the tank creates an interferometric and stationary pattern, in that the internal water interface works as a mirror to the acoustic waves. Then, the optical coils capture the ultrasound intensities present in their fixed positions, modulating light beams through their photo-elastic (acousto-optic) effects, creating an output signal from which the values of amplitudes and phases are extracted.
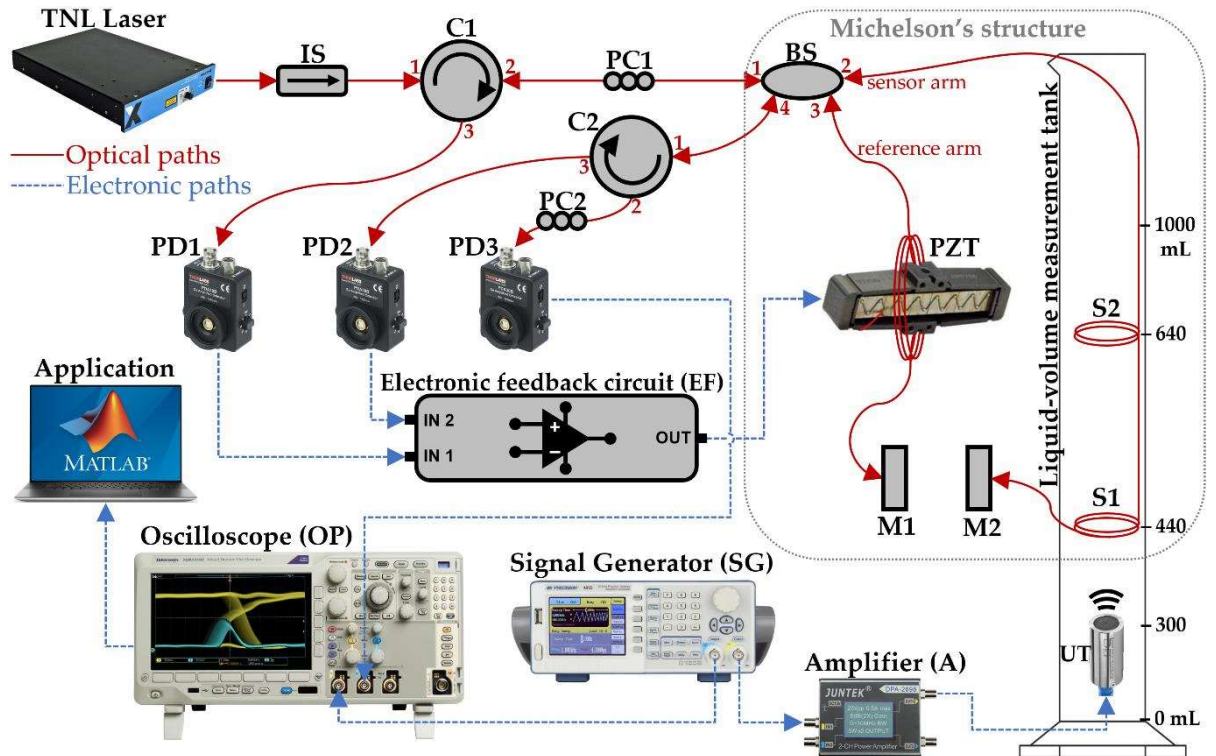
Figure 4. Fiber-optic hydrophone (FOH) system setup. TNL Laser at 1550 nm; IS – optical isolator; C1 and C2 – optical circulators; BS –beam splitter; PC1 and PC2 – polarization controllers; PD1, PD2 and PD3 – photodetectors; M1 and M2 – Faraday's mirrors; PZT – piezoelectric actuator wound by an optical fiber coil; S1 and S2 – optical fiber coil sensors; UT – ultrasound transducer; EF – electronic feedback loop circuit; OP – oscilloscope; SG – signal generator; A – 3 dB amplifier; Application is a software developed in Matlab; Liquid-volumes measurement tank.

Figure 5 shows the laboratory arrangement including all hardware components used by the experimental setup of the FOH system.
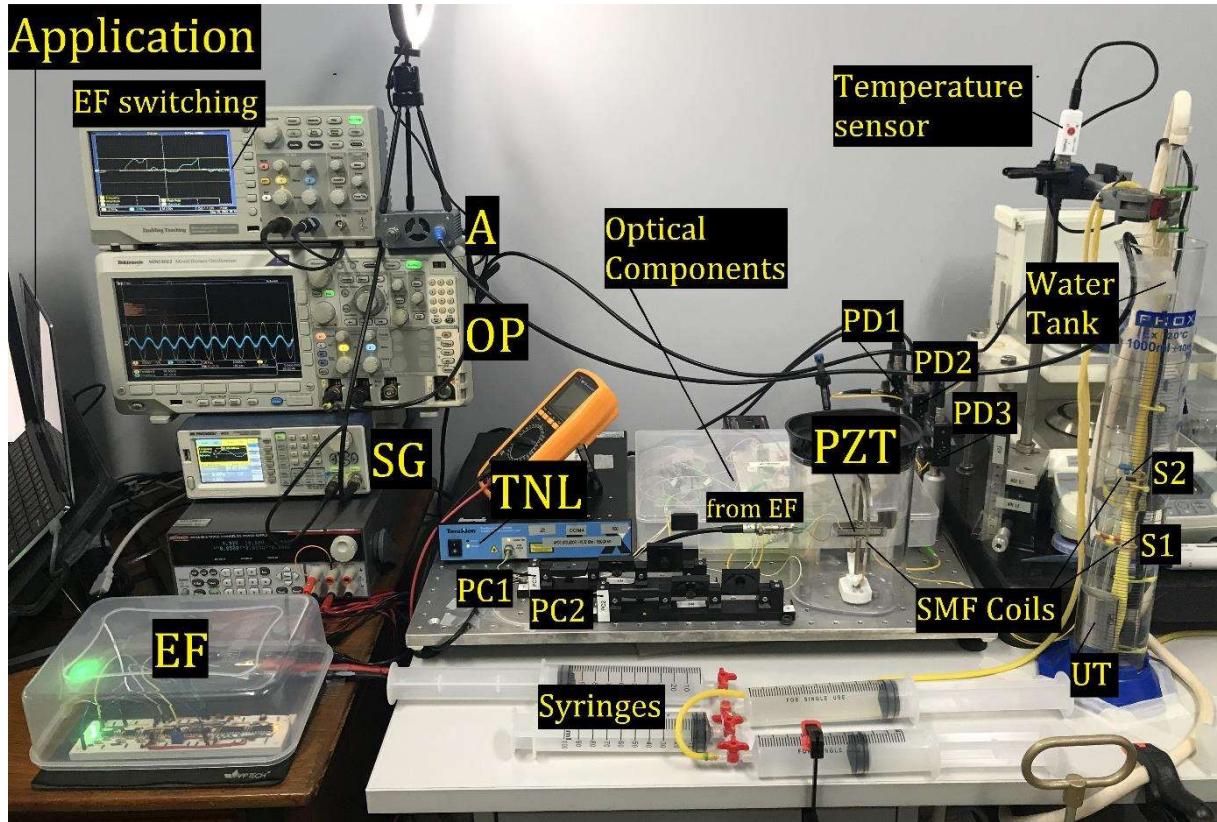
Figure 5. Laboratory arrangement of hardware of the setup components.

It is not trivial to mathematically equate the components of this setup to reach an expression that would infer the water's liquid volumes by using the system's output. This setup involves optical and acoustic phenomena taking place simultaneously, by an unbalanced MI composed by two optical coils in the same sensor arm, with noises stabilized by an EF circuit driving a piezoelectric actuator in the reference arm. The coils are not multiplexed.

3.2   HARDWARE COMPONENTS

The setup worked for seven days in an air-conditioned room and water's temperatures varying from 22 °C to 24 °C. The test tank is a graduated measuring cylinder glass of 1000 ml, with 10 ml grading divisions, filled with water one milliliter at a time, with a syringe graduated at 1 ml, from 440 ml to 1000 ml (561 liquid-volume points). The measurements started at 440 ml due to setup arrangements and positioning of the UT inside and in the bottom of the tank. The irradiating face of the UT was positioned at the 300 ml volume due to its mechanical size. And the distance of 140 ml between the UT's face and first coil S1 was due the near field of Fresnel's zone.

A coherent laser light source TN Laser (Teraxion Narrow Linewidth Laser) is tunned at 1550 nm, and

its wavelength drift is negligible as it implements internal hardware for electronic current and temperature stabilization. The TNL laser injects 12.5 dBm of light power in the system. The isolator IS (Thorlabs) protects the laser source port against undesired returning power. After passing through circulator C1, polarization controller PC1 and the 3 dB beam splitter BS, the light power is equally injected in both MI arms, what are ended by the Faraday-rotator mirrors M1 and M2. The MI's reference arm is composed by an optical coil of 11 meters (XIE; CHEN; REN, 2009) made with SMF fiber (Corning SMF-125/9, only with acrylate protection) wound around a piezoelectric actuator PZT (Thorlabs APF705), responsible for the stabilization mechanism, as seen in Figure 6 (a). As the PZT component was brand new and taken from the box to be used for the first time, it was not characterized of calibrated.

The sensor arm's coils S1 and S2 are shown in Figure 6 (b) and (c), they are both identical and made by the same fiber type, with an outer diameter of 2.4 cm, and 25 fiber turns, resulting in 188.5 cm of total fiber length per coil. The number of turns and diameter of the optical coil are defined by the total length of fiber section L_c intended to be exposed to the acoustic fields, as expressed in Equation (10). In total, considering all fibers used, components connections, installation arrangements and coils, each MI arm achieved a length around 15 meters. Single mode fibers were used because the behavior and analysis of multimode interferometers are difficult to control (ELEZOV et al., 2018).
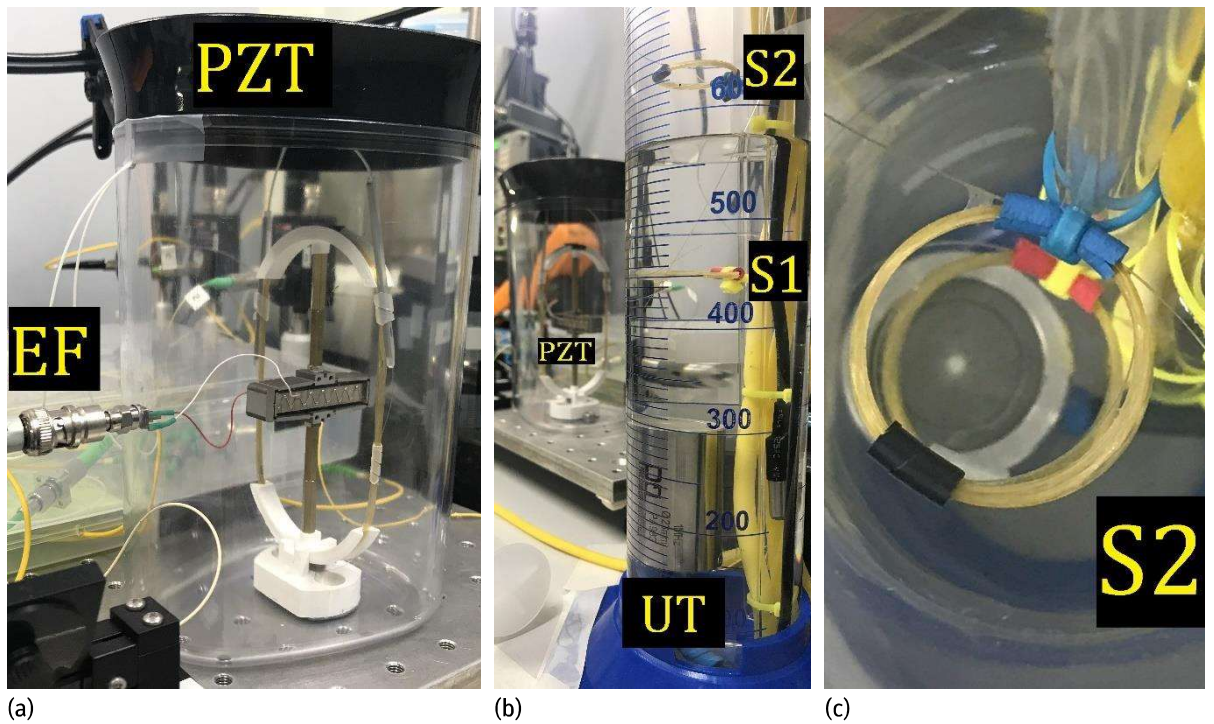
Figure 6. (a) Fiber coil wound around the piezoelectric actuator responsible for the stabilization mechanism; (b) Water tank showing the UT source at the bottom, and the optical fiber coil sensors S1 and S2 above; (c) Top view of the optical coil sensor S2 seen from the top of the water tank.

All optical components, as the isolator, circulators, beam splitter, faraday mirrors and PZT with its

optical coil were installed inside boxes (non-hermetic) with the goal of mitigating external influences such as temperature variations, random pressure fluctuations, sounds, air flows, or mechanical stress on fibers and connectors. The optical components and photodetectors were mounted over an optical bread board with rubber foot to mitigate mechanical vibrations, and vibrations on the table where the components are settled. These disturbances are controlled as they can decrease the measurand accuracy (CHANG; ZHU; YANG, 2015; ELEZOV et al., 2018; XIE; CHEN; REN, 2009).

Although the use of polarization controllers in this system is not a mandatory requisite, the PC1 was placed at the MI input to improve contrast (ELEZOV et al., 2018), and, following the same idea, the PC2 was installed at the MI output which delivers the sensor's measurand signal to the photodetector PD3. The two circulators C1 and C2 provide the required optical paths (XIE; CHEN; REN, 2009) to photodetectors PD1, PD2, and PD3 (Thorlabs PDA30B-EC). This optical arrangement with both circulators guarantees that the inputted optical signals to PD1 and PD2 are 180° out of phase.

While both photodetectors PD1 and PD2 are only working for the stabilization mechanism, PD3 is uniquely responsible to supply the sensor system's outputted signal. The EF circuit is fed by PD1 and PD2, and its output drives the PZT, which stretches the optical coil of the MI's reference arm, keeping the interferometer as much as working around the quadrature state, and providing a final sensing signal with less interferences through PD3. The quadrature state stability can be experimentally expressed by the standard deviations of the main sensor measurands, for a fixed liquid volume, while the system is working under empirical external noises. These values are presented in the results section of this dissertation.

On the electronic side, the Signal Generator SG (BK Precision 4053) is set to provide a 100 kHz continuous sinusoidal wave (CW) on its both output channels, CH1 and CH2, with the same phases, but different peak-to-peak voltages of 10 Vpp and 1.8 Vpp, respectively. During the preliminary tests, a range of UT frequencies were evaluated from 50 kHz to 1 MHz, and an adequate response range of voltage and phase variations occurred at 100 kHz. The lower UT (Precision Acoustics Unfocussed 1 MHz, 23 mm diameter and 75 mm focal distance) frequency was used to allow higher sound wavelengths in the water, supplying a better response to the volume variations of 1 ml.

The SG-CH1 signal is amplified by the Juntek DPA-2698 (BW 10 MHz and 3 dB gain) amplifier (A), which outputs a 20 Vpp sinusoidal CW signal of 5 W to the UT. The second port of signal generator SG-CH2 was connected to the CH1 input of the Oscilloscope OP (Tektronix Open Choice MDO 3012), to work as a reference for the FOH system phase recovery. The UT is positioned in such a way that the ultrasound waves are irradiated upwards through the liquid and their wavefronts are parallel to the plane of the optical coils S1 and S2. The FOH output is injected to the second oscilloscope port (OP-CH2).

Both OP ports (CH1 and CH2) were configured to supply AC coupling and BW of 20 MHz, making them more adequate to the involved frequencies, and to cut DC power. The OP's Fourier Transform function

allows seeing one channel in both time and frequency domains, simultaneously, and the signal amplitude of 1.8 Vpp from SG-CH2 was chosen to help adjustments during the setup construction.

Last, the Matlab Application (MA) (THE MATH WORKS INC., 2021) reads the signals from both oscilloscope ports and extracts two measurands: amplitude in volts and phase in degrees. This phase value is calculated by MA and stands for the difference between the original signal injected to the UT (interferometer input) and the resulting signal delivered by PD3 (main MI output). This output is then digitalized by the oscilloscope at a sample rate of 100 MS/s, the samples are read in vectors of ten thousand points of double type variables, which are passed through a software band-pass filter, and then to a Fourier Transformation, from which the values of amplitude and phase are registered in a database.

3.3   FRESNEL'S ACOUSTIC NEAR FIELD

A Fresnel's near field was kept free between the UT surface and the first coil S1. The acoustic's near field is a Fresnel's space that should not be obstructed by any object so that the acoustic field (RUPITSCH, 1992) emitted by the UT is not destroyed or severely attenuated, what would compromise the acoustic detections by the optical coils in the MI's sensor head. The calculation of this field considers the UT's diameter ($D = 23$ mm), the ultrasound frequency ($f = 100$ kHz), and the wave speed in water (LUBBERS; GRAAFF, 1998). As the lower temperature, the larger near field, the worst case of T = 22 °C was used to calculate the water's sound speed s_{wa} (LUBBERS; GRAAFF, 1998) and the near field distance F_{nf} (RUPITSCH, 1992), as follows:

$$s_{wa} = 1404.3 + 4.7 * T - 0.04 * T^2 = 1488.34 \ [m/s] \tag{15}$$

The near field for a cylindrical UT is expressed by:

$$F_{nf} = \frac{\left(\frac{D}{2}\right)^2}{\lambda_{wa}} = \frac{\left(\frac{23 * 10^{-3}}{2}\right)^2}{\lambda_{wa}} \ \therefore \ \lambda_{wa} = \frac{s_{wa}}{f} = \frac{1488.34}{100 * 10^3} \ \therefore \ F_{nf} = 8.9 \ [mm] \tag{16}$$

For the test tank of this experiment and $\lambda_{wa} = 14.9$ [mm], the distance $F_{nf} = 8.9$ [mm] is equivalent to the volume range $F_{nf} = 26.3$ [ml]. Considering that the UT surface is placed at the volume of 300 ml, the near field for $f = 100$ kHz and T = 22 °C is found in the range from 300 ml to 326.3 ml and, therefore no objects, not even an optical coil sensor, should be put in this region.

As higher ultrasound frequencies were also used during the preliminary tests, the free water volume of 140 ml purposely left between the UT surface and the first S1 coil allows the use of a maximum frequency of 520 kHz, without obstructing the near field.

3.4 ELECTRONIC FEEDBACK LOOP CIRCUIT

In this work, an active and self-compensate mechanism for the MI was adopted to control the environment disturbances and offer a better stability to the measurand data produced perceived by the sensor head. It was based in the work developed by (XIE; CHEN; REN, 2009) and (CHANG; ZHU; YANG, 2015), that implemented the electronic feedback (EF) loop circuit scheme shown in Figure 7, whose hardware prototype is shown in Figure 8.
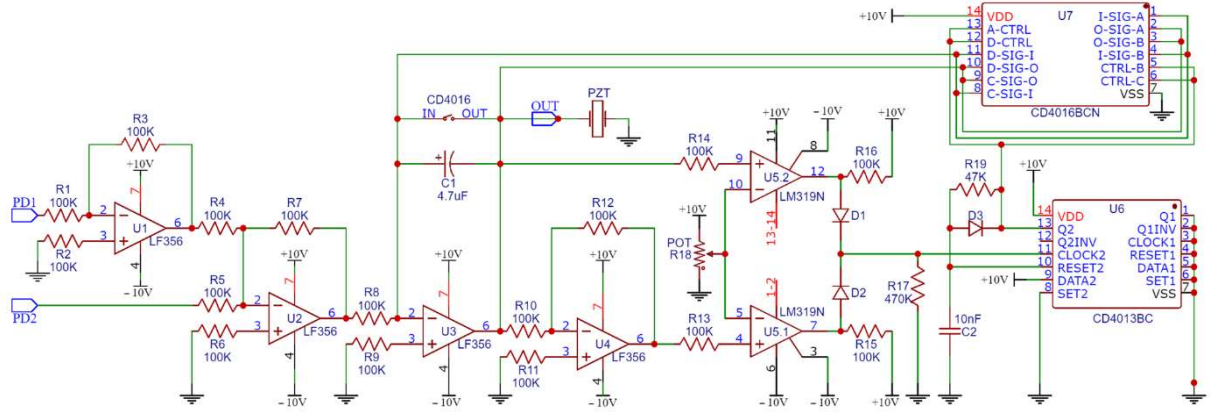
Figure 7. Schematic of electronic feedback (EF) loop circuit for Michelson's stabilization.
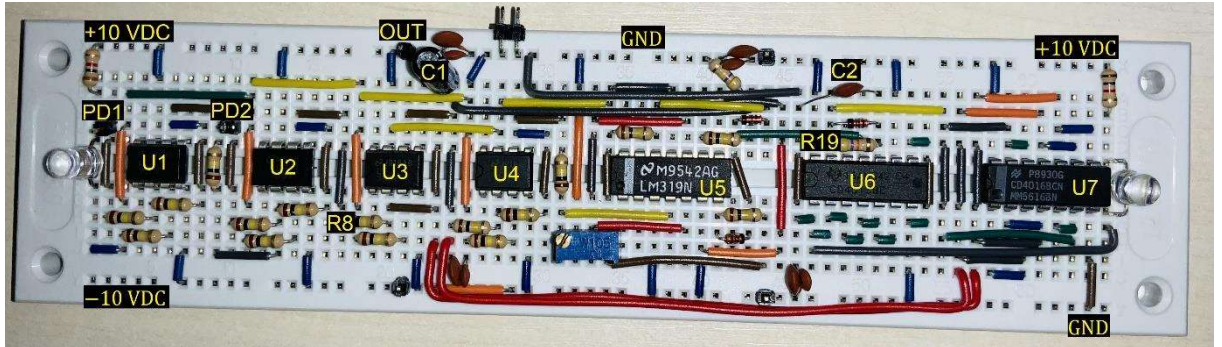
Figure 8. Prototype of the electronic feedback (EF) loop circuit for Michelson's stabilization.

Although the EF loop was mounted on a noise-prone breadboard, it was not a problem for the FOH prototype as that circuit is projected to work under low frequencies, around 25 Hz in maximum. The EF is composed by four operational amplifiers chips (U1 to U4), a dual comparator chip U5, a dual flip-flop chip U6 (CD4013BC), one four-electronic keys chip U7 (CD4016BCN), and other discrete components like resistors (18 units), capacitors (2 units), and diodes (3 units). This EF circuit has two inputs whose signals are received from the photodetectors PD1 and PD2, and one signal output, which drives the PZT. The output values of PD1 and PD2 are matched through knobs of dB gains adjustments of the photodetector's hardware (Thorlabs PDA30B-EC).

Some minor changes have been made to the original author's electronics and optical schemes published by (XIE; CHEN; REN, 2009) to simplify the setup, but without affecting any original functionality of

the circuit. Both input low pass filters were not electronically implemented as they were provided by the oscilloscope input ports and by a software high-pass filter implemented in Matlab. Furthermore, the DC power suppliers were simplified to use the values of +10 and −10 volts, cutting the need of +5/−5 and +15/−15 VDC inputs. Finally, the four U7 electronic switches were connected in parallel to decrease their internal resistance and allow a properly PZT operation.

The active stabilization's EF loop acts as an homodyne demodulator that nullifies as much as possible the output of the differential amplifier U3, locking the MI operation around the vicinities of the quadrature point (KIRKENDALL; DANDRIDGE, 2004). The interferometric signals outputted by PD1 and PD2 (electronic currents) are 180° out of phase and inputted to the EF circuit for differential detection.

$$I_{PD1} = I_0[1 + K_0 \cos{(\phi_s + \phi_d)}], \tag{17}$$

$$I_{PD2} = I_0[1 + K_0 \cos{(\phi_s + \phi_d + \pi)}], \tag{18}$$

where I_0 relates to the system input power, K_0 is related to the interferometric fringe visibility, ϕ_s is the static differential phase, and ϕ_d is the disturbances differential phase.

After PD1 output is inverted by U1, and, together with PD2 output, both signals are differentially combined by the converter U2, the following signal is seen on the U2 output, where K_2 if the conversion gain of U2:

$$U2_{OUT} = K_2 * \cos{(\phi_s + \phi_d)} \tag{19}$$

After $U2_{OUT}$ is integrated by U3, the new output signal is presented below, where K_3 is the conversion gain of U3:

$$U3_{OUT} = K_3 * \sin{(\phi_s + \phi_d - \pi/2)} \tag{20}$$

As the perfect quadrature point is defined by $\phi_s + \phi_d = \pi/2$, and the interferometer is forced to be kept around the quadrature state, then $U3_{OUT}$ will tend to zero, knowing that the differential phase will be:

$$\Delta\phi = \phi_s + \phi_d - \pi/2 \therefore \Delta\phi \cong 0 \tag{21}$$

However, this absolute zero is not supported, and in the vicinities of the quadrature point, the differential phase $\Delta\phi$ drifts assume small values, allowing the approximation below, considering that $\sin{(\Delta\phi)} \cong \Delta\phi$, for small values of the angle $\Delta\phi$:

$$U3_{OUT} = K_3 * \sin{(\Delta\phi)} \therefore U3_{OUT} \cong K_3 * \Delta\phi, \tag{22}$$

This simplification represents a practical assumption when a sine or cosine math function falls inside a cosine or sine formula, like the term '$\exp{i(\omega_0 t + K_a \sin(\omega_a t) + \phi_0)}$' in Equation (9). This assumption is considered valid for $\Delta\phi \ll 1$ and a value of $\Delta\phi \leq 0.1$ radians is described as acceptable by (UDD; WILLIAM B. SPILLMAN, 2011). In fact, it avoids the need of considering many terms of the Bessel's functions

of the first kind, as the first two terms of their coefficients' family, $J_0(\Delta\phi)$ and $J_1(\Delta\phi)$, represent 98% of the homodyne power spectrum energy (UDD; WILLIAM B. SPILLMAN, 2011).

Therefore, $U3_{OUT}$ is quasi-linear at the quadrature state (CHANG; ZHU; YANG, 2015). It is used as the correction signal that drives the PZT making displacements and strain changes in the optical fiber coil wound around it, keeping the interferometer working close to the quadrature state.

The EF circuit also tracks the external noise through an equivalent voltage in capacitor C1. The circuits U5.1 and U5.2 compare C1 with the reference voltage defined by the potentiometer POT (R18) and, when they get equal, the EF switches the C1 voltage to zero, by an up pulse to flip-flop U6, that keeps the four U7 switches closed and discharging by the time of $\tau = R19 * C2 = 0.47$ [ms]. The reference value of +5 volts is selected with R18 (potentiometer), so that the limits of +5/−5 volts of accumulated phase drifts errors are enough to protect the PZT and other electronic components, respecting their technical datasheets (CHANG; ZHU; YANG, 2015). In general, the EF circuit can be regarded as a high-pass filter with a cut off angular frequency f_{EF} in Hertz, as expressed by (XIE; CHEN; REN, 2009):

$$f_{EF} = \frac{K_p K_d}{2\pi * R8 * C1} \tag{23}$$

The voltage-phase coefficient K_p [rad/V] for PZT actuator and its optical fiber coil, and the phase-voltage coefficient K_d [V/rad] for photodetectors have been experimentally measured by driving the PZT with a low frequency triangular wave (XIE; CHEN; REN, 2009), allowing the calculation of f_{EF} [Hz], and are presented further in the results section.

3.5   SENSITIVITY, RESOLUTION, BANDWIDTH AND OTHER TECHNICAL CHARACTERISTICS

The purposed setup is composed by different elements, both in optical and electric domains, each with specific technical parameters of power, frequency, bandwidth, sensitivity, resolution, internal noise sources, and others (KIRKENDALL; DANDRIDGE, 2004). The purposed FOH system's sensitivities, resolutions and bandwidth are dependent on the setup's arrangement and on its components' intrinsic characteristics, whose values are examined in the results section, following collected data series and their derivatives of phases and amplitudes.

Although it has not been the scope of this work to measure isolate parameters of the optical coils built for the MI's sensor head, other studies have already demonstrated a sensitivity of −116 dB *re* rad/μPa in the bandwidth of 10 Hz to 2 kHz, phase noise of −102 dB *re* rad/$\sqrt{Hz}$, and pressure noise of 14 dB *re* μPa/$\sqrt{Hz}$ (MENG et al., 2021). Other study shows a sensitivity of −170 dB *re* rad/μPa, noise floor of 50 dB *re* μPa/$\sqrt{Hz}$ below 1 kHz (KIRKENDALL; DANDRIDGE, 2004).

These parameters vary with the type and length of fibers exposed to the acoustic waves, coil sizes

and their layout, number of fiber layers, acoustic wave frequency and direction, mechanical and elastoop-tic properties of fibers, and other parameters (BUCARO; HICKMAN, 1979; JARZYNSKI; HUGHES, 1980; MONSAY; GILBERT, 1981; WANG, C. C. et al., 1994).

3.6   DATA COLLECTION AND DATABASE STRUCTURE

The MA developed to this experiment is online connected to all setup equipment and took twenty measurements of amplitude and phase per each milliliter of liquid-volume, counting a total of 11220 read-ings (561 milliliter steps x 20 readings per milliliter) that were stored in a database. The system spends 3 (three) seconds to collect and process one reading, therefore, the twenty samples of a milliliter require a minute to be processed. Values of amplitudes (volts) were rounded to 2 digits, and phases (degrees) were rounded to zero digits, to the right of the decimal point, so to allow the system to calculate the modes (most frequent values) of both measurands.

Each reading was registered as a tuple of data object (lines) having 64 columns of data (features). Among these features, the tuple has the point values of amplitude and phase, besides their modes, means, standard deviations, and outlier indicators. A tuple also carries features for both intermediate and final values of modes and means. Twenty measures compose a group, and the intermediate values are calcu-lated based on the measurements taken until the moment of a point collection. For example, the 12th meas-urement of a group registers intermediate values of means and modes for the twelve measures taken until that moment. The last measure of a group is calculated after removing the interquartile outliers. In this work, these outliers are those values greater than 1.5 times the interquartile size, above the upper quartile (75%) and below the lower quartile (25%), for a measurement group. The interquartile method is applicable for both data normally distributed or not. The database also registers a boolean feature to show outliers that were less than 10% or above 90% percentile ranges. This 10%-90% range has been empirically chosen just to be different from the interquartile strategy, and, at the same time, to not be so aggressive with outliers exclusions, as it keeps 80% of the data collected for a milliliter volume point. These two strategies are referred in the text as 'interquartile' and 'percentile' outliers, respectively.

As the temperature changes the acoustic properties of the liquids, each object tuple also has a fea-ture that registers the water's temperature, whose value is provided by an electronic sensor installed in-side the test tank and connected to the MA. This feature was used by the machine learning algorithms with the merely action of adding it, or not, among the features selected to compose a data model to be as-sessed. Also, no phase or amplitude values from repetitive cycles of increasing and decreasing volumes were registered in the database, despite the fact this repeatability was seen during the setup tests.

The entire process of collecting data took thirty-three hours distributed among six days, from which six Excel files were exported each day by Matlab in '.xlsb' extension, with sizes ranging from 313 to 998

kbytes. After grouping all Excel files and providing some initial data treatment, the final database of the FOH system was exported as a Matlab file in '.mat' extension, with 25 Mbytes of size. This file contains a table of 11220 data tuples with 64 features each.

3.7   PHASE AND AMPLITUDE DATA SERIES ANALYSES

This work presents data series analyses of amplitudes and phases, including their derivatives in relation to liquid-volumes. Standard deviations and small linear intervals of these series have been evaluated. All graphs show results before and after S2 coil is submerged. The data series include the mode values of each measurand. First, the phase and amplitude are individually analyzed, and further both are put together in a two-dimensional cartesian space. A specific phase analysis included three adjustment actions, after which an unwrapped phase characterization has been obtained for the FOH system.

A limitation in the arctangent function executed by homodyne detectors, where sine and cosine signals are converted to phase, is that the phase can change a maximum of π radians between samples. So, changes greater than π represent an ambiguity as to whether the signal travelled a full clockwise or counterclockwise lap around the four quadrants (WANG, L. et al., 2006). Therefore, an absolute change higher than 180° between two adjacent milliliters may be a discontinuity caused by a new wrap cycle in the domain of 360°, influenced not only by the intrinsic nature of the system but also by noises that are still present in the measured data, despite the stabilization mechanism. Under this condition, predictive algorithms could be used to improve upon the π limitation (KIRKENDALL; DANDRIDGE, 2004), as performed by other publications about phase measurands from optical interferometers (HU; LI; LIU, 2017; SATTAR et al., 2020; WANG, L. et al., 2006).

3.8   THREE ACTIONS OF PHASE SERIES ADJUSTMENTS

Taking into consideration the aspects of phase detection reported in the earlier topic, three actions have been applied on the phase collected data of this work.

3.8.1   Action (a) – Fixing Phase Discontinuities with 360° Rotations

In action (a), all absolute variations above 180°, between two adjacent milliliters, were rotated by 360°. For example, if a liquid-volume point is −270° and the earlier point was +45°, then a 315° absolute variation is detected and, therefore, the −270° point is changed to +90°, after a 360° rotation. If this new value also causes new further absolute variations above 180°, the respective liquid volumes were rotated as well.

3.8.2 Action (b) – Unwrapping the Phase Series

In action (b), the phase data series is unwrapped in which the angles are rotated by ±180° based on the following thresholds' vector: [−180° −90° −60° −30°]. The minus signal of a threshold value works only on the up-down variations, and the plus signal on the down-up variations. The algorithm runs on each phase difference between two adjacent milliliters, and if it is higher than the threshold value and it is in the signal direction of the threshold signal, the point and the remaining series are rotated by 180°. Up-down movements are rotated by +180° and down-up by −180°. In the end, these rotations perform an unwrap operation in the whole phase series, respecting the arctangent function properties, as the earlier and the updated angles still keep the same tangent values. Different values of this vector were assessed, and it has been found that positive thresholds (high down-up movements) did not affect the unwrapping process.

3.8.3 Action (c) – Excluding Phase Points with Deviations Above 60°

In action (c), as a strategy of phase noise treatment, a phase point was excluded when the standard deviation in the measurements group of liquid-volumes was greater than 60° during the data collection.

3.9 FITTING MODEL FOR THE PHASE CHARACTERIZATION

After performing the three actions of phase adjustments, the best result was selected based on the greater R^2 (R-Squared) and minor RMSE (root mean square error), according to the fitting model assessed for the final series of unwrapped phase. Among the models evaluated, there were polynomials, exponentials, Fourier series, gaussians, power series and sum of sines.

The RMSE and RMSE% are calculated by Equations (24) and (25) respectively, where Y_{Ti} and Y_{Pi} are the truth and predicted values, respectively, of the ith term in the phase series composed by N terms.

$$RMSE = \sqrt{\frac{1}{N} \sum_{i=1}^{N} (Y_{Ti} - Y_{Pi})^2}\,, \tag{24}$$

$$RMSE\% = \sqrt{\frac{1}{N} \sum_{i=1}^{N} \left(\frac{Y_{Ti} - Y_{Pi}}{Y_{Ti}}\right)^2} * 100\%, \tag{25}$$

3.10 TWO DISTANCE-BASED ALGORITHMS AND FIVE DISTANCE-METRICS

This work employed machine learning algorithms under supervised learning to predict liquid vol-

umes from amplitudes and phases of acoustic waves. Two distance-based techniques were tested, Rocchio and k-NN (ROGERS; GIROLAMI, 2017), with five distance metrics: Euclidean, Mahalanobis, Cosine Distance, Cosine Similarity, and Manhattan. The Rocchio is a classifier based on the centroids calculated from the training data, and defining which centroid is closer to a tested data point. The k-NN is based on the k-nearest tested point neighbors to the training data points. Although both Rocchio and k-NN are similar for being distance-based algorithms, they are slightly different in the way each one uses the training and the test points. However, both employs the same math to calculate distances between two points in multidimensional spaces.

In total, six scenarios have been evaluated, and each scenario is defined by a specific choice of object tuples (lines) and attributes (features) from the 11220 x 64 matrix of collected data. A group of selected tuples defines a dataset, and the group of selected attributes defines a data model. In this case, a data model can include, per example, the water's temperature attribute, so to see the influence of this filed in the results. Also, each scenario has its own criteria to separate the training from the testing datasets. As an example, a training dataset can be composed only by the twentieth object tuple of the liquid-volume points (mode centroids), and the testing dataset by the remaining objects. Or, yet the training can be composed by a random choice of 75% of all tuples and the testing dataset includes the remaining 25%. In addition, other characteristics, like the distance metrics used and the 'k' number of neighbors in k-NN have been assessed.

When the training dataset is composed by one tuple standing for the centroid of a milliliter, both Rocchio and 1-NN reach the same accuracy. So, in these cases, the 3-NN is presented, while other cases used 1-NN as it delivered better accuracies. For all scenarios evaluated, both training and testing datasets were standardized to avoid distortions caused by the scales of the attributes. Each liquid-volume point was defined as a class (label) with which new aleatory sample of phase and amplitude is processed to obtain the respective liquid volume. The data is balanced as the classes have the same number of samples, although it can vary a little with scenarios that applied outlier exclusions.

3.11 GAUSSIAN PROCESS REGRESSION

In addition to the use of clustering algorithms, this work also assessed machine learning regression versions based on the same fitting models used to characterize the unwrapped phase data series. However, instead of testing only the mode values of amplitudes and phases, the regression models with machine learning were applied to all database points with the same random selection of 75%/25% to define the training and the testing datasets, respectively. The best result in terms of R2 and RMSE was obtained from the Gaussian Process Regression (GPR), whose values are presented in the result section of this paper.

4   RESULTS AND DISCUSSION

4.1   ELECTRONIC SIGNALS OUTPUTTED BY THE FOH SYSTEM

This results and discussion section starts with the presentation of an instant example of both electronic signals inputted and outputted from the FOH system, as they are originally shown on the oscilloscope screen, so to provide a view of the physical attributes that were extracted from these signals, explained by the balloons of Figure 9, and how the output signal becomes unstable and without quality, when the active stabilization provided by the EF loop is deactivated, as shown in Figure 10.
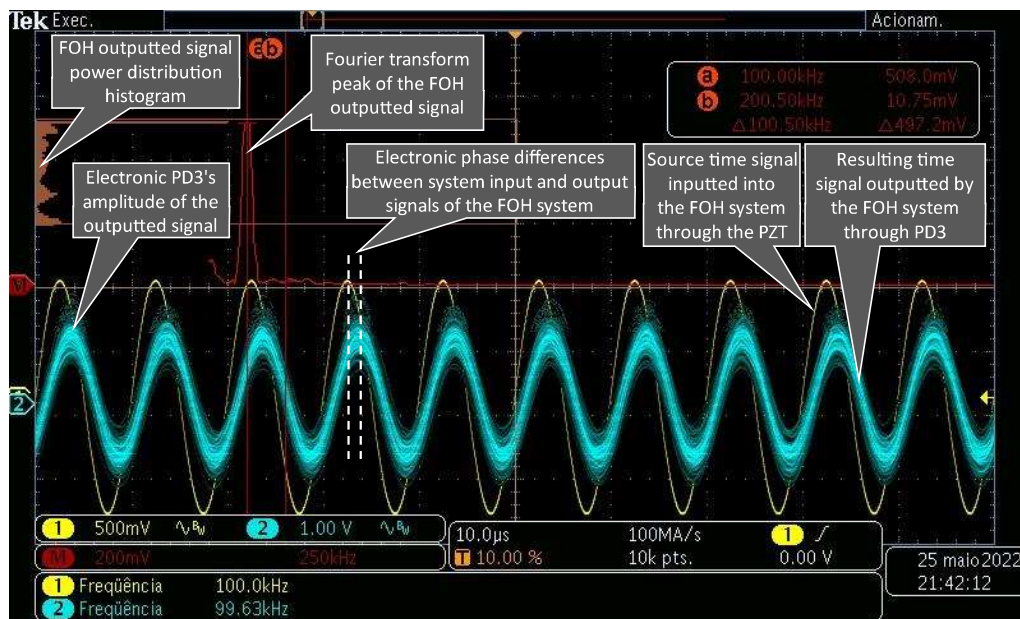

Figure 9. Oscilloscope screen of the FOH electronic signals with active stabilization (EF loop is on).
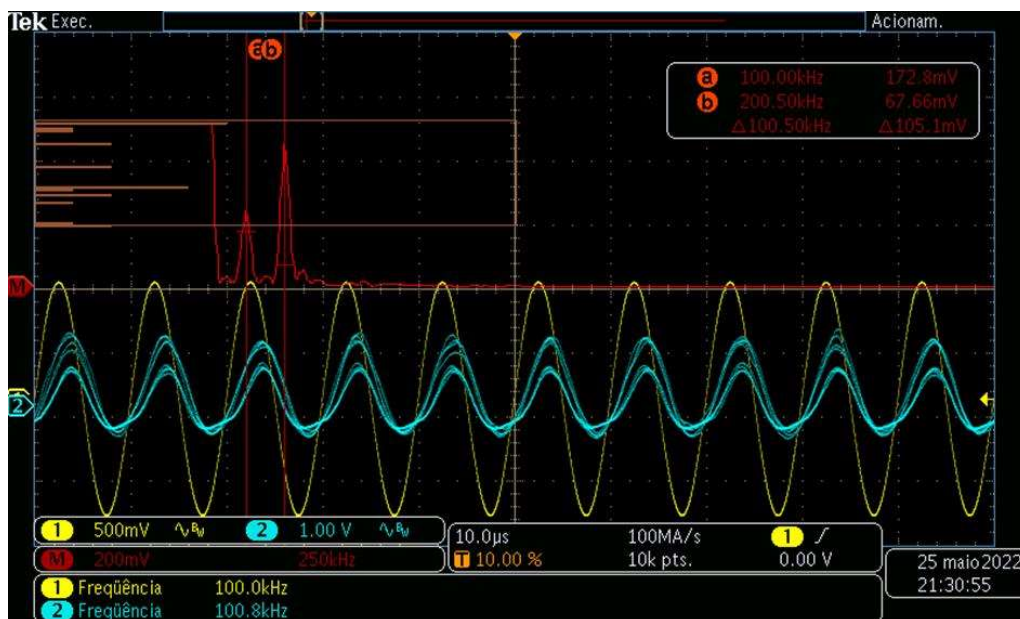

Figure 10. Oscilloscope screen of the FOH electronic signals without active stabilization (EF loop is off).

When the stabilization mechanism is off, the environment noise levels make the sensor system useless, as the measurand information is lost. It is demonstrated by Figure 10, as the energy outputted by PD3 is unstable and spread among other harmonics (see the high level of energy on the second harmonic of 200 kHz), the power histogram becomes undefined, and the system cannot provide a minimally stable value for the amplitude and electronic phase measurands. On the other hand, as shown in Figure 9, when the active stabilization is on, the amplitudes and electronic phases are more stable, can be measured, and processed to be associated with their respective liquid volume.

4.2 SENSITIVITY, RESOLUTION, BANDWIDTH AND OTHER TECHNICAL CHARACTERISTICS

The FOH system has been designed to operate at the fixed acoustic frequency of 100 kHz with an ultrasound transducer able to work at the maximum frequency of 1.5 MHz. The Figure 11 shows an experimental result of a 6 dB bandwidth of 700 kHz, ranging from around 30 kHz to 730 kHz, inside which specific frequencies of 80 kHz, 220 kHz, and 340 kHz have presented high peak values in the response curve. This response has been computed under a fixed liquid volume, as different volumes present different voltage amplitudes for a fixed frequency. The choose of FOH system's fixed operation frequency has considered this experimental bandwidth, the Fresnel's zone restrictions, and the longest possible acoustic wavelength in the water.
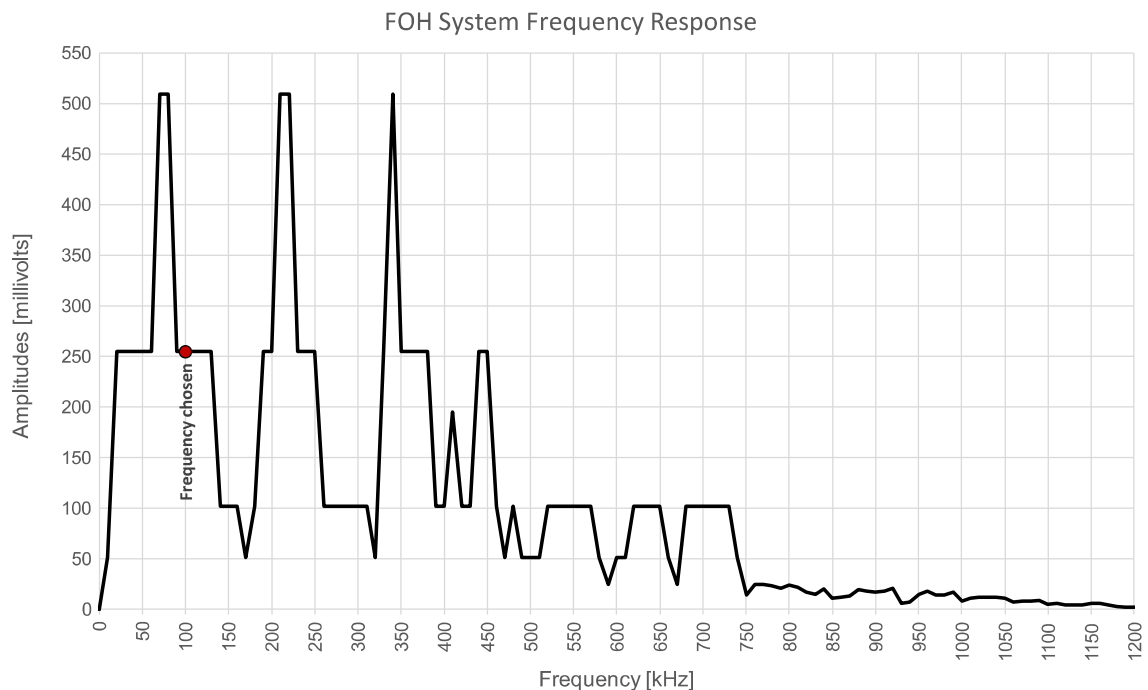

Figure 11. Experimental FOH system's ultrasound frequency response curve.

The EF loop circuit cutoff bandwidth is calculated following (XIE; CHEN; REN, 2009), and Figure 12 shows the oscilloscope graphical results used to obtain the sensitivity $K_p = \frac{31.5\pi}{4.24} = 23.34$ [rad/V] and

$K_d = \frac{1.06}{\pi/2} = 0.67$ [V/rad], after driving the PZT with a 50 Hz and V_{pp} = 4.24 V triangular wave. The only requirement to choose the triangular wave's frequency is to make it as small as possible in order to allow counting the number of cycles in the resulting sinus modulated wave. Therefore, the experimental high cutoff frequency of EF loop circuit resulted in $f_{EF} = \frac{23.34*0.67}{2\pi*100*10^3*4.7*10^{-6}} = 5.33$ [Hz], what was enough to mitigate most environmental noises. A replacement of capacitor C1 from 4.7 μF to 1 μF raises this value to 25.07 Hz, what is close to the value of 21.65 Hz experimentally found by (XIE; CHEN; REN, 2009).
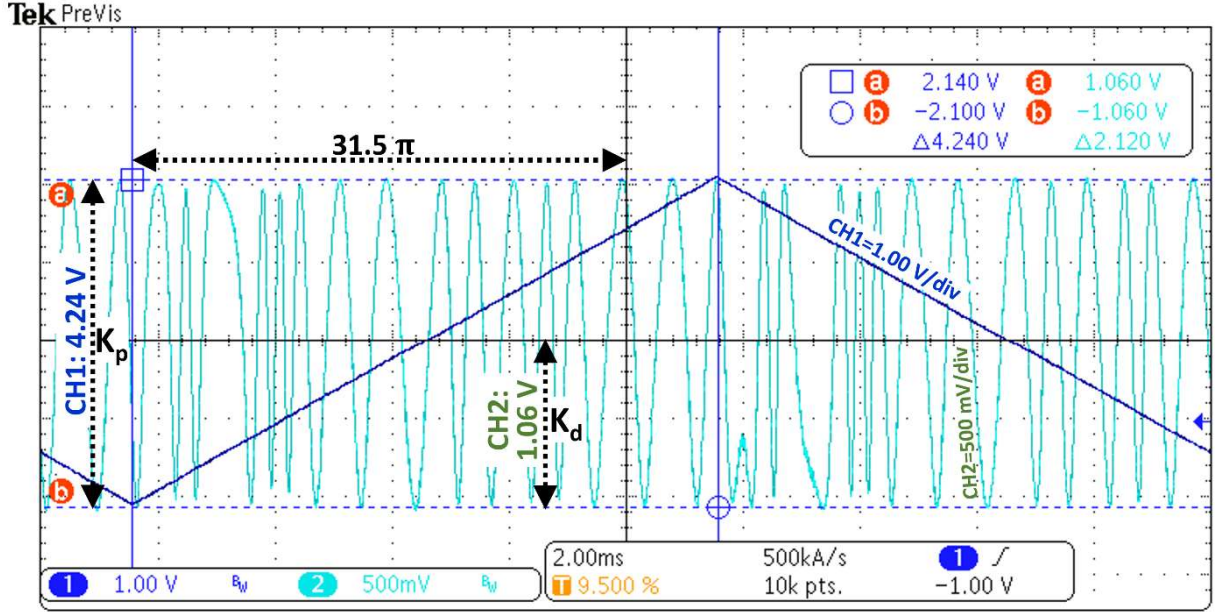
Figure 12. Coefficients K_p (PZT with optical coil) and K_d (photodiodes) experimentally obtained.

4.3 ORIGINAL AMPLITUDE AND PHASE DATA SERIES COLLECTED

The original collected values of amplitudes and phases per each liquid-volume point are plotted in Figure 13. As a homodyne detector (phasemeter), each amplitude in volts stands for the optical phase displacement between the signals from the MI's arms, related to a specific liquid-volume. And each phase point is the electronic acoustic phase difference between the inputted and the outputted signals from the FOH system. Phasemeters recover the phases from the four-quadrant arctangent, according to the ratio between two quadrature signals (a sine and a cosine). The relation between the expected phase and the phase effectively measured should be linear, but there are often distortions caused by spurious effects in the optics or in the signal-processing, that result in the non-linearities and periodic errors (WATCHI et al., 2018) seen in Figure 13.

Figure 13. Original amplitude and phase mode values collected per milliliter.

Specific characteristics can be noted from the original collected data. Both amplitude and phase series are non-linear with liquid volumes; they are not intrinsically correlated to each other; there are different peaks and valleys when only S1 is under water, then when both S1 and S2 are submerged; below S2, the phase varies around t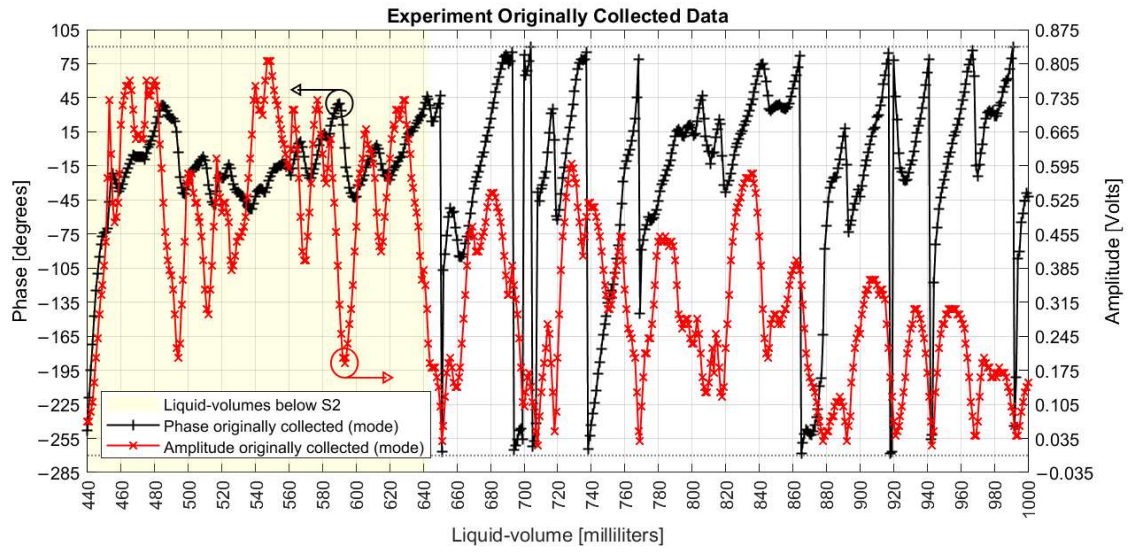he limits of −45° to +45° degrees, covering a range of 90°, as limited by the quadrature ; above S2, the phase measurand shows maximum and minimum values that touch the limits of −270° and +90°, covering a range of 360°; above S2, the amplitude window of peaks and valleys dislocates down; both series present limited linearity intervals with liquid volumes, as seen in Figure 14; the amplitude shows quadratic behaviors at volumes of 820, 890, 920, 940 and 970 ml; the phase measures show discontinuity jumps near the volumes of 650, 690 to 710, 740, 860, 920, 940 and 990 ml; and, the first measured phase at 440 ml presented a value smaller than −180°.

These results confirm non-linearities, differences of using one or two optical coils as sensing elements, attenuation of acoustic fields as the volume of water increases, and phase differences between the optical signals in the MI arms are not related to the phase differences between the acoustic signal inputted and outputted from the system.

4.4   PHASE MEASURAND ANALYSIS

Three actions were applied on the phase collected data in order to: (a) fix the discontinuities; (b) unwarp the data series; and (c) mitigate the noises.

In action (a), after all rotations, the new phase profile is shown in Figure 14, from which it is noted the effect of dislocating the the whole data series from the limits of −270°/+90°, to a new range of −180°/+180°.
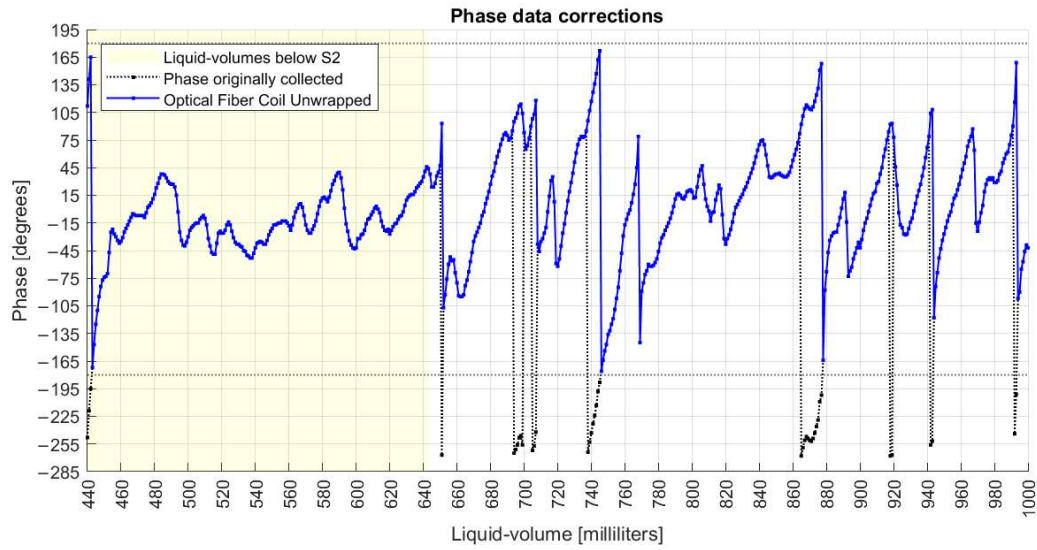
Figure 14. Phase measurand with corrections of discontinuity jumps ≥ 180°.

For a comparison purpose with the original data presented before, Figure 15 shows the original amplitudes and the new phases series corrected with the 360° rotations.
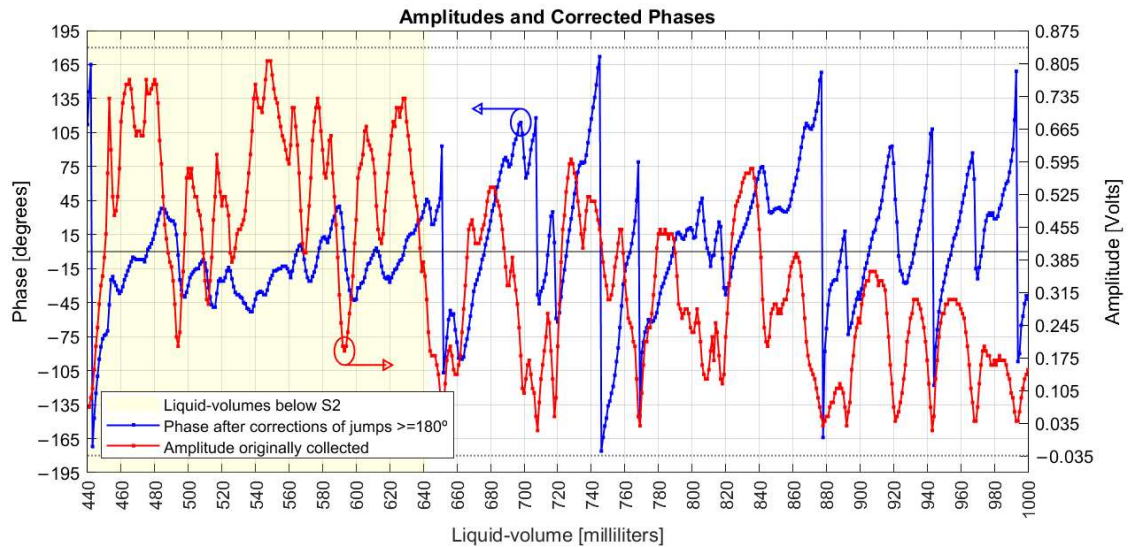
Figure 15. Original amplitudes and corrected phases.

A derivative analysis of both amplitude and phase measurands are presented in Figure 16, with common phase sensitivities reaching 20° degrees/ml (349 milliradian/ml) and amplitude in 70 mV/ml. The dashed lines are the one standard deviations over means, of both measurands, separated by liquid-volumes below and above S2 coil. Comparing the variations due to influence of S2 coil, the amplitude deviation decreased from 44 mV to 31 mV, while the phase increased from 24° to 37°.

That is, the presence of S2 decreased the sensitivity of amplitude (homodyne detection related to the optical phase differences between the signals inside the MI arms) but increased the sensitivity of the acoustic phases (related to the electrical phase differences between the signal inputted to the UT and the measurand signal delivered by PD3). Based on that result, a future analysis would take S2 out of the system

45

and verify if coil S1 alone would detect different series of amplitudes and phases, including their derivatives as well.
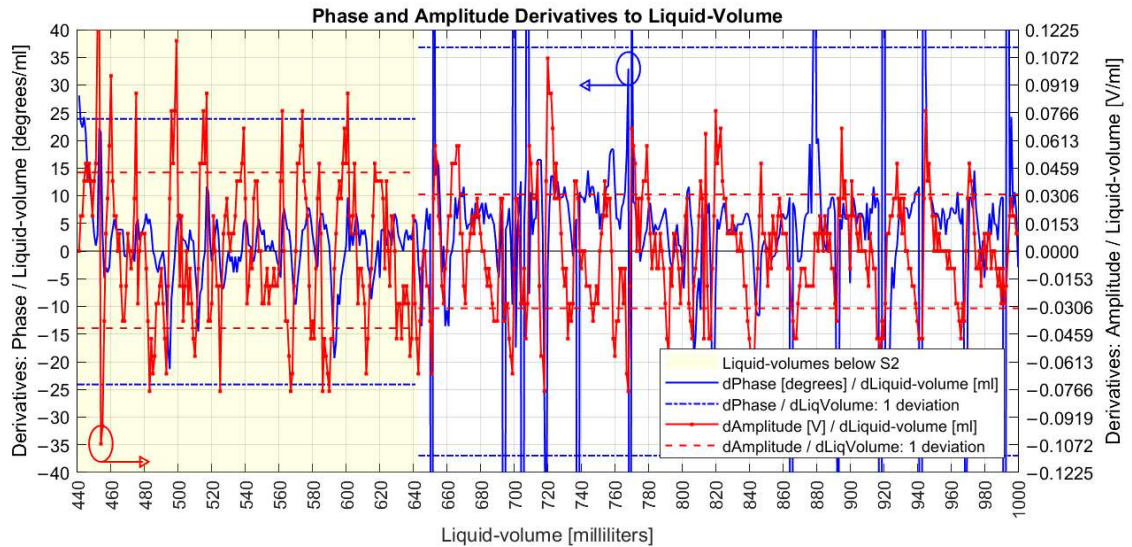
Figure 16. Derivatives of amplitudes and corrected phases.

Figure 17 shows plain linear intervals with numbers at the ends of straight lines being the first and final liquid-volume of each interval. This figure also shows that the majority of phase points have their mode values ('x') closed to their mean values' ('+') symbols, what is a characteristic of normal distributions, although neither normal fitting test was performed over the data, as it was not a goal of this work.
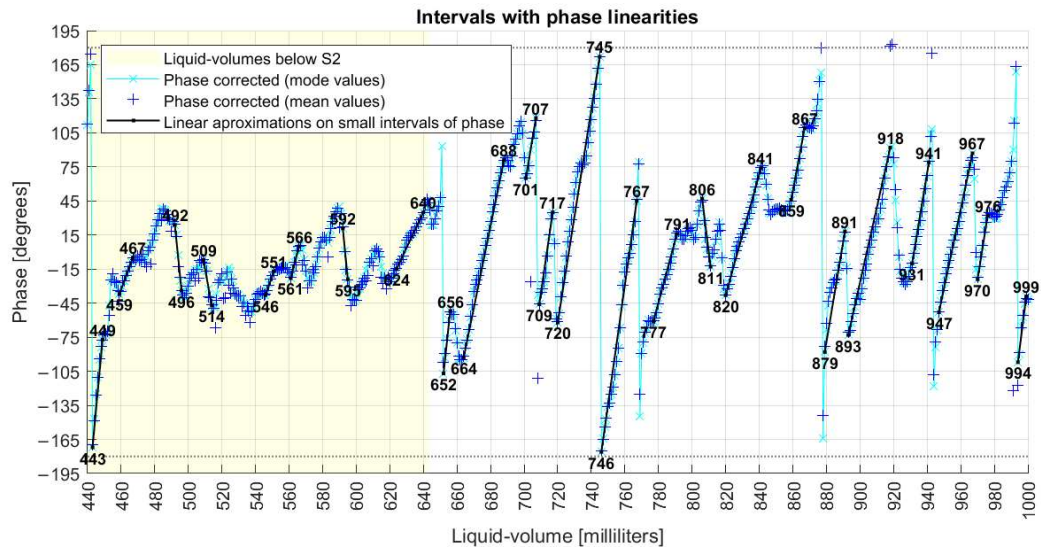
Figure 17. Liquid-volume intervals with linearities with phase.

Figure 16 shows that after executing action (a), the phase derivatives series are mostly confined in the limits of −20°/20°, with one standard deviation of 37°. So, a maximum admissible standard deviation error of 60° for a point in the action (c) is a conservative value, although other values have been evaluated. So, the action (c) caused the elimination of 4% of collected data and Figure 18 shows the resulting series after each one of the three phase actions were executed. The bottom of Figure 18 also shows the room's

and water's temperatures, both measured during the data collection days represented by small circles on the graph.
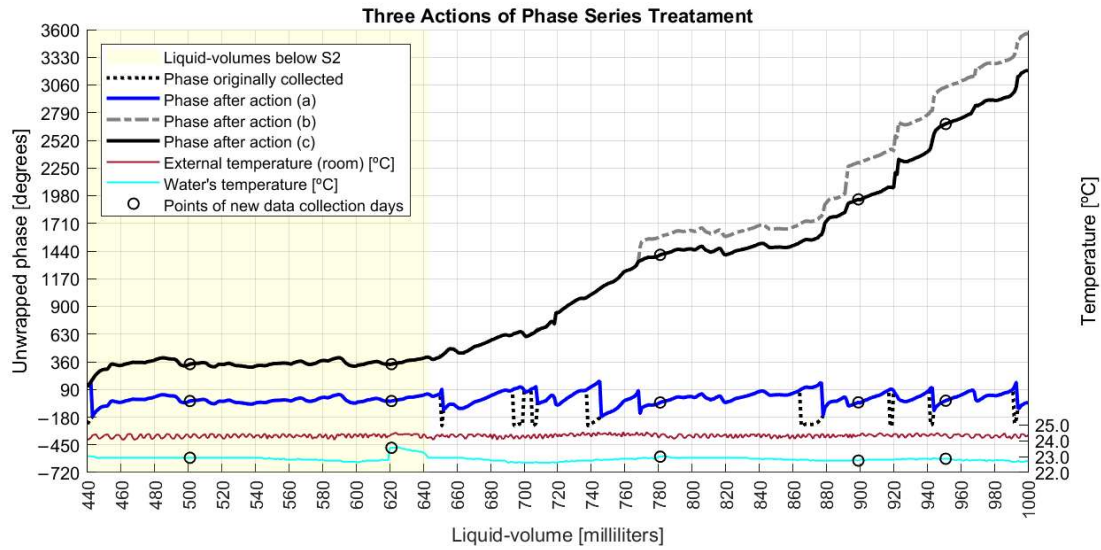
Figure 18. Three actions of phase series adjustments.

According to Figure 19, while the original phase derivatives reached a six-standard deviation of 290°, the final adjusted phase series ended with a six-sigma deviation of 82°. This result was achieved after the execution of the three sequenced steps of phase adjustments, whose algorithms improved upon the π constraints of angles measurands (KIRKENDALL; DANDRIDGE, 2004).

In fact, those steps have detected and cleaned phase jumpers between adjacent milliliters, with absolute values higher than 180°, and unwrapped the phase series after removing phase points with deviations equal or greater than 60°, from the original data.

The derivative analysis shows the improvements achieved by these purposed phase adjustments algorithms, which had the goal of finding a final phase characterization for the FOH system. Those actions have been based on parameters that can be previously configured, allowing the MA to apply them as long as new data are online collected.
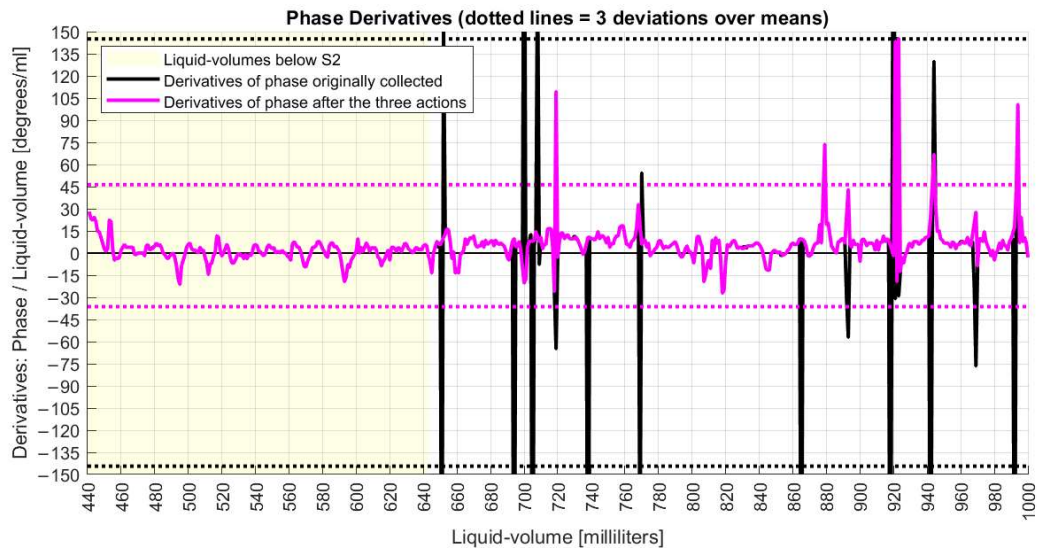
Figure 19. Derivative analyses of phase signals before and after corrections

Finally, Figure 20 shows the phase characterization after fitting the unwrapped phase with a sum of sines of nine terms, resulting in the R2 of 0.9994, and the RMSE% of 4.15%. The model was configured to run with least absolute residual method and non-linear least squares.
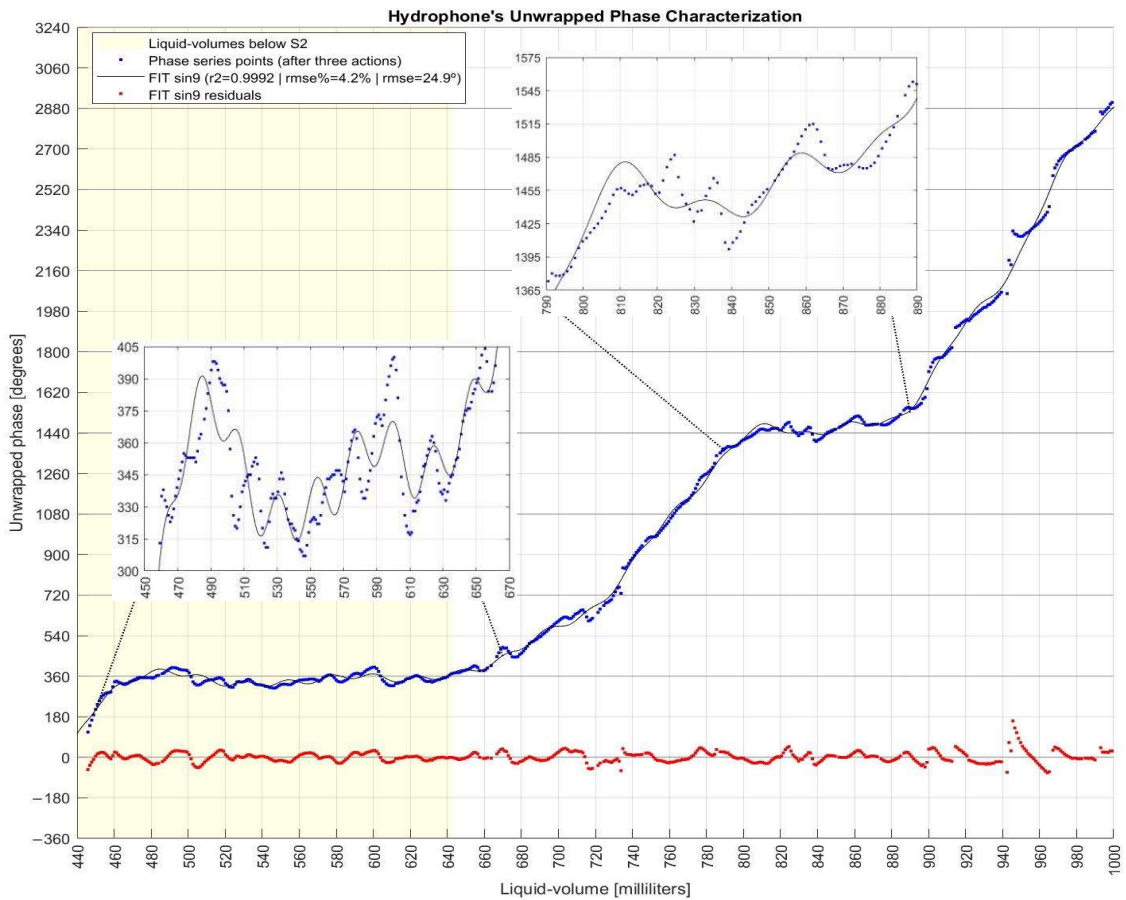
Figure 20. Hydrophone system's unwrapped phase characterization.

The sum of sines fitting function is expressed by:

$$L_{ml} = \sum_{i=1}^{9} \mathbf{a_i} * \sin(\mathbf{b_i} * \Delta\emptyset_s + \mathbf{c_i}), \qquad (26)$$

where L_{ml} is the predicted liquid-volume in milliliters and $\Delta\emptyset_s$ is the angle detected and processed by the FOH system's application, after the three actions of phase treatments are applied. The coefficients a_i, b_i and c_i of the adjusted function are listed in Table 2.

Table 2. Coefficients of sum of sines fitting function.

i	a_i	b_i	c_i
1	2419	0.7729	0.7455
2	1087	1.66	−2.039
3	288.9	3.401	0.8193
4	102.6	5.768	−0.8964
5	29.65	9.122	−2.307
6	5518	18.81	−1.821
7	5517	18.81	1.317
8	−4.334	13.82	9.008
9	13.23	45.2	−0.7065

4.5 AMPLITUDE MEASURAND ANALYSIS

The amplitude and its derivatives series have already been presented in the earlier section, to allow their comparison with the phase series. So, a next analysis is to show the presence of linear intervals, as shown in Figure 21. This figure also shows that most amplitude points have mode values quasi-equal to mean values, what is also a characteristic of normal distributions.
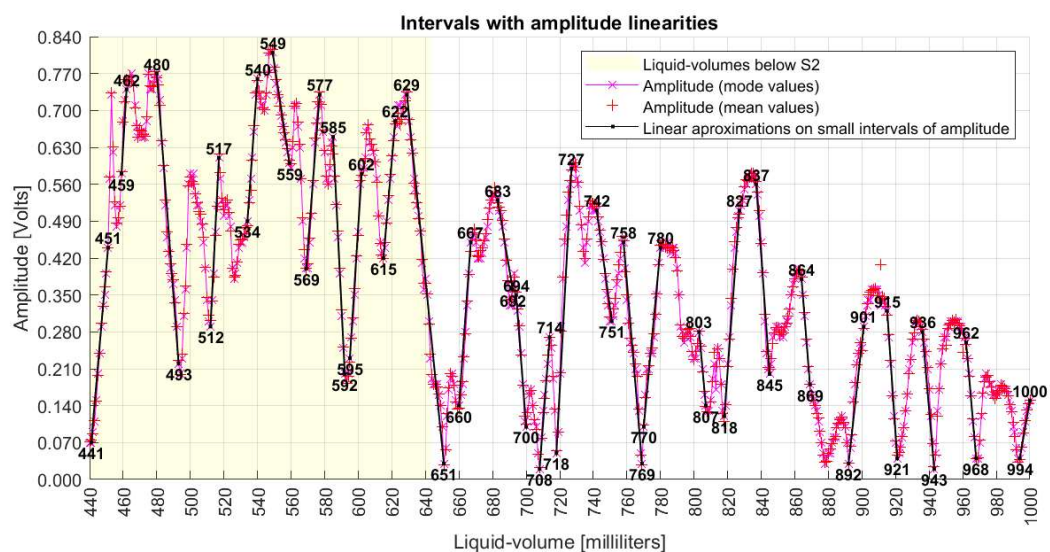
Figure 21. Liquid-volumes with linear intervals on the amplitude series.

Figure 22 shows the derivatives of amplitude to liquid-volumes, with limited ranges of linear behavior.
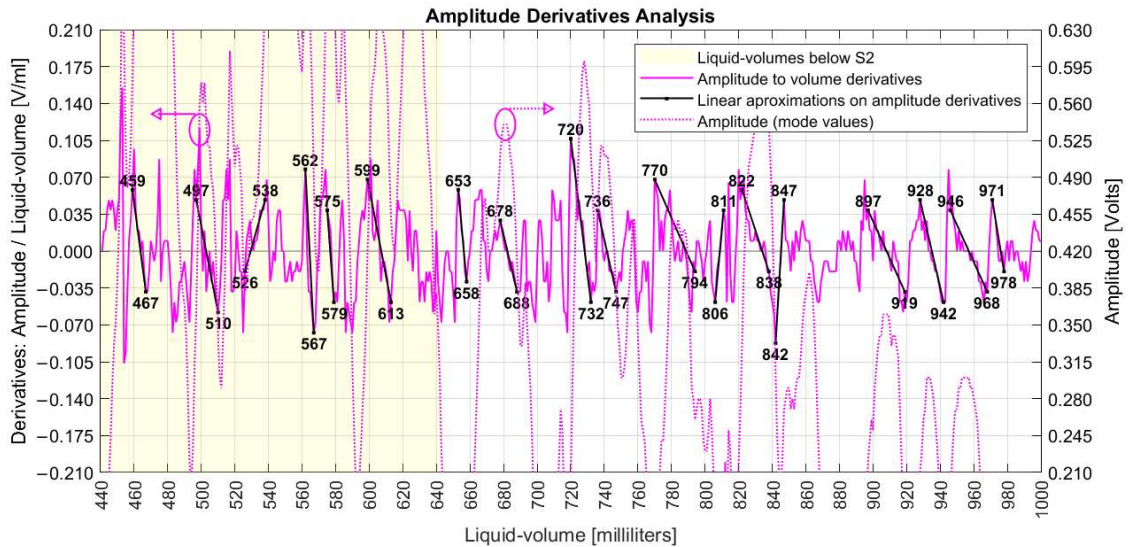
Figure 22. Liquid-volumes with linear intervals on the derivative of amplitude series.

The amplitude analysis shows that the collected data is non-linear, and it is not obvious to derive a math function standing for a system that could fit to this data behavior. In this sense, next section presents an analysis using both phase and amplitude mode points.

4.6   PHASE AND AMPLITUDE DATA SERIES ANALYSIS (MODE VALUES)

This topic evaluates both amplitude and phase as coordinates of a two-dimensional cartesian space. Figure 23 uses the corrected phases previously presented in Figure 14, and Figure 24 use the unwrapped phases presented in Figure 20. Both graphs have the phase measurand in the 'x' axis, and the amplitude measurand in the 'y' axis, with point coordinates defined by their mode values. The integer numbers plotted over the sequenced points are the respective liquid-volumes in milliliters. Considering the substantial number of measured points, not all values were plotted to preserve an adequate graphical visualization by the reader.

Figure 23 shows points standing for a linear sequence of liquid volumes, but evolute as curves of amplitude and phase coordinates, making clockwise turns, as long as the liquid volume increases linearly, forming drawing patterns like 'snail paths' that are overlapped by other paths, showing a non-linear behavior of the FOH system. This pattern also shows spaces with a high concentration of liquid-volume points and empty spaces in the vicinities. There is also a difference in space points occupations when S1 is submerged, (liquid volumes below S2), then when both S1 and S2 are under water. In fact, the unwrapped phases are seen only with measurements above S2.

Figure 23. The 2-D grade of amplitudes and corrected phases (only action 'a' applied).

Figure 24. The 2-D grade of amplitudes and unwrapped phases (after action 'c' is applied).
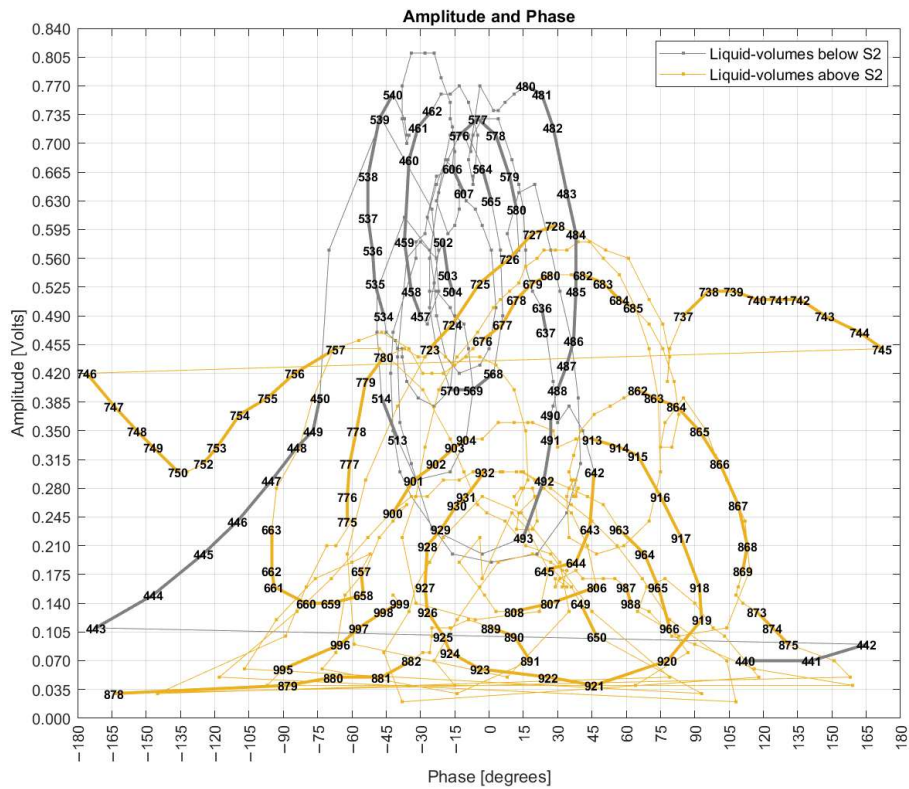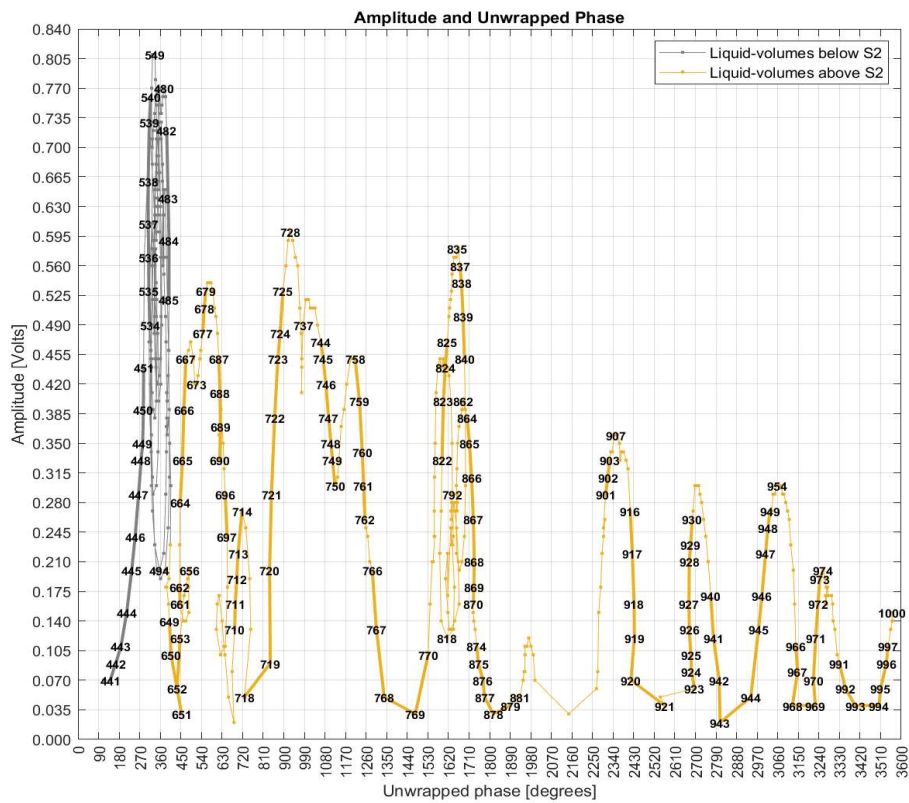
4.7   ROCCHIO AND K-NN WITH DIFFERENT DISTANCE METRICS

This topic presents six scenarios of data analyses. Scenarios one to four used the phase adjusted to the range of −180°/+180°. Scenario five used the unwrapped phase and scenario six used the original phase collected, without any phase adjustments.

Figure 25 shows the results of first scenario that evaluated the mode values of phase and amplitude regarded to a liquid volume point. The mode values were used as the training dataset, and they were evaluated against themselves as testing data. In this scenario, an accuracy of 100% was expected, but the accuracy of 96.8% shows that 3.2% of the centroids are overlapped, that is, although they stand for different liquid volumes, they have the same coordinates of amplitude and phase. This result corroborates the behavior of Figure 23 in which the 'snail paths' overlap each other more than one time. This also shows that Rocchio is not applicable if data is composed by centroids of mode values. Additionally, k-NN can be seen as useless with an accuracy of 31.2%. The small circles in the graphs supply a visual notion of the wrong classified points.

This first Rocchio's result shows a trade-off decision in which the need of rounding numbers to allow the use of mode values has a collateral effect of increasing the probability of centroids overlapping. So, the number of digits to the right of the decimal points is an input parameter to the system. The fewer digits, the higher probability of overlapping. Based on this first scenario results, new data models and new selections of training and testing data were defined to improve the analyses.
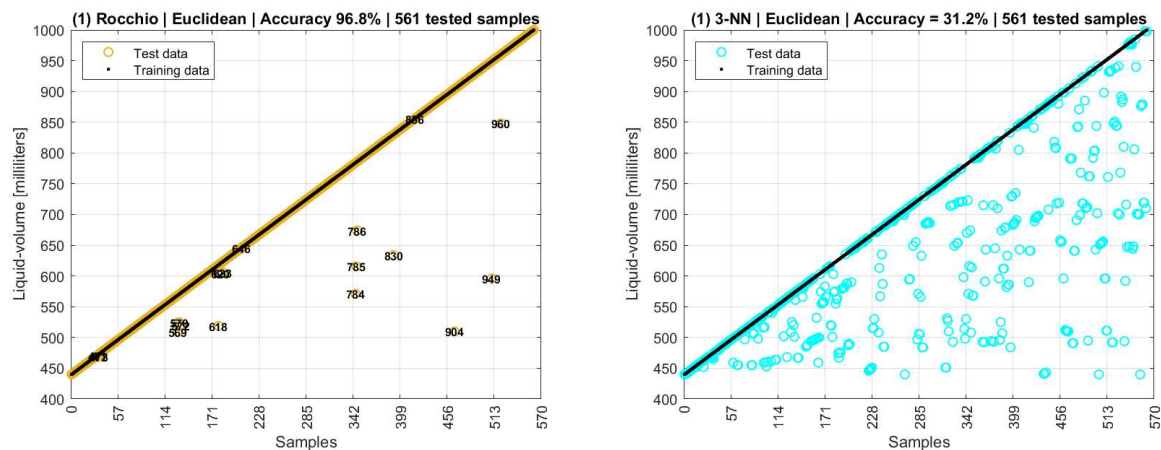
Figure 25. Rocchio and k-NN accuracies with centroids of mode values.

A second scenario used the same data model of the first one, but with modes replaced by means, and Figure 26 shows accuracy of 100% for Rocchio and 29.8% for 3-NN.
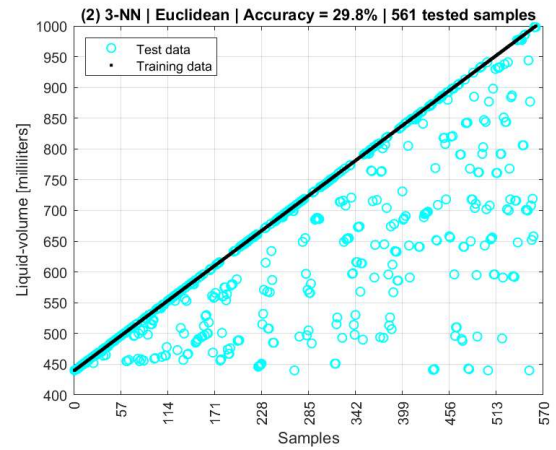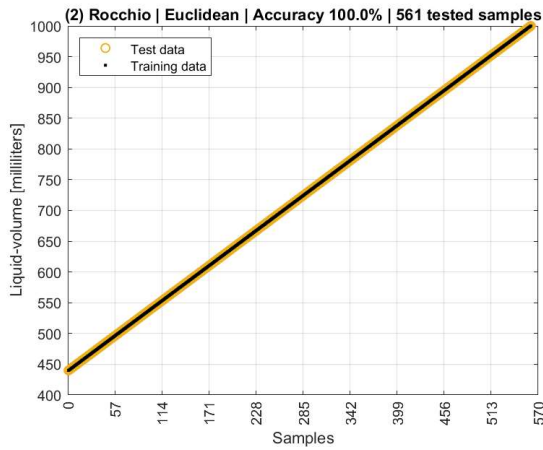
Figure 26. Rocchio and k-NN accuracies with centroids of mean values.

If both modes and means are used in the data model as a third scenario, the Rocchio and 3-NN accuracies are 100% and 31.4% respectively. A partial conclusion here is that both training and testing datasets, besides the data models, are still needed to be improved. Figure 27 shows a fourth scenario in which the training data are the centroids of modes and means, of phase and amplitude, and the testing data are all the remaining points collected by the experiment setup, excluding the centroids and the inter-quartile outliers.
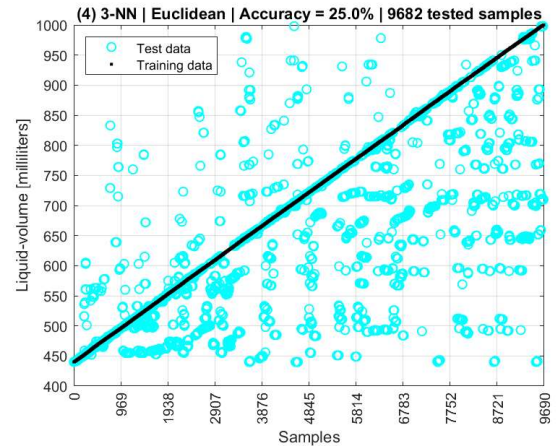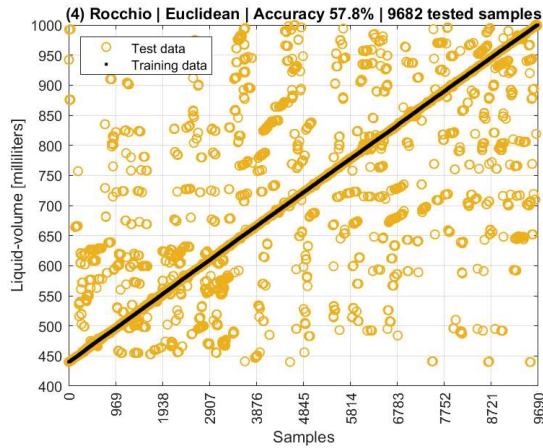
Figure 27. Rocchio and k-NN accuracies with complete datasets and excluding outliers.

The fourth scenario is more data intensive than the third's, as it used more tuples as testing data, resulting in an accuracy of 57.8% for Rocchio and 25.0% for 3-NN. Additionally, the 5-NN's accuracy is 15.8%. In this sense, it is possible to note that training datasets composed only by the centroids are poor data models as their low distances and overlapping points are not adequate to distance-based algorithms.

Therefore, a fifth scenario has been defined, in which the data model was improved and had its attributes composed by point values, means and modes (intermediate and finals), for both amplitude and phase, complemented by the water temperature. The fifth scenario considered the unwrapped and characterized phase data presented in Figure 20.

53

The choice of object tuples (lines) was aleatory to define the training and the testing datasets with the respective proportion of 75%/25%. Initially, no outliers have been excluded. The k-NN was defined to one nearest neighborhood (1-NN) as it presented better results than when using three or more neighbors for all distance metrics.

As a result, for Euclidean distance, 1-NN reached an accuracy of 91.6% and other k-NN with three or more neighbors presented lower accuracies (3-NN=87.9%; 5-NN=85.3%; 9-NN=80.2%; 15-NN=71.6%; and 20-NN=64.0%), reinforcing that 1-NN is always better.

Figure 28 shows the resulting accuracies for different distance metrics used with Rocchio and k-NN, in that the 1-NN with Manhattan distance reached the accuracy value of 97.0%. The 'Cosine Similarity' metrics resulted in accuracies of 0% (zero) for both algorithms and for all scenarios evaluated so far.
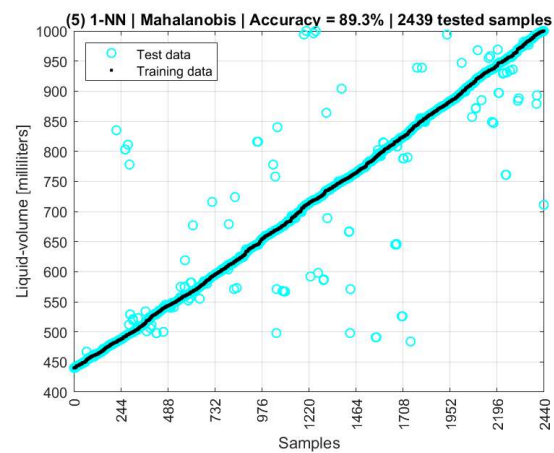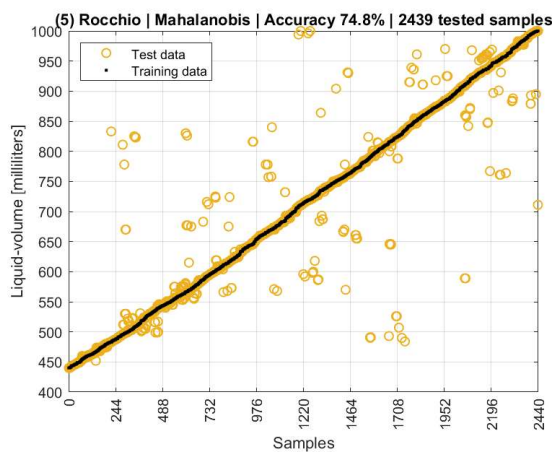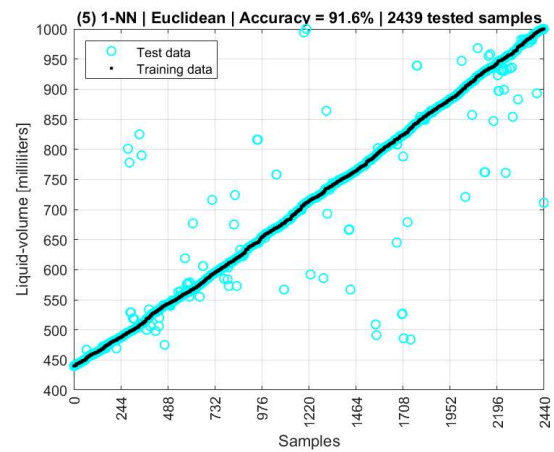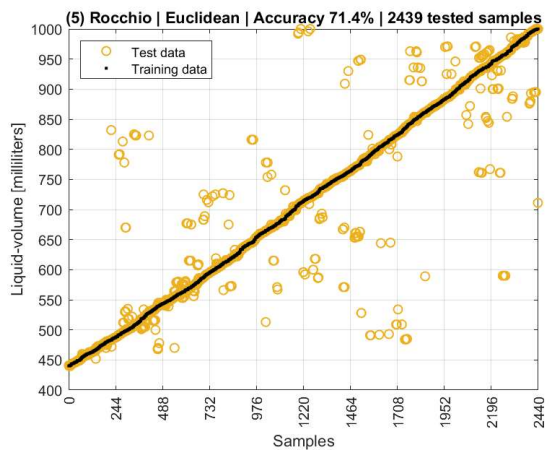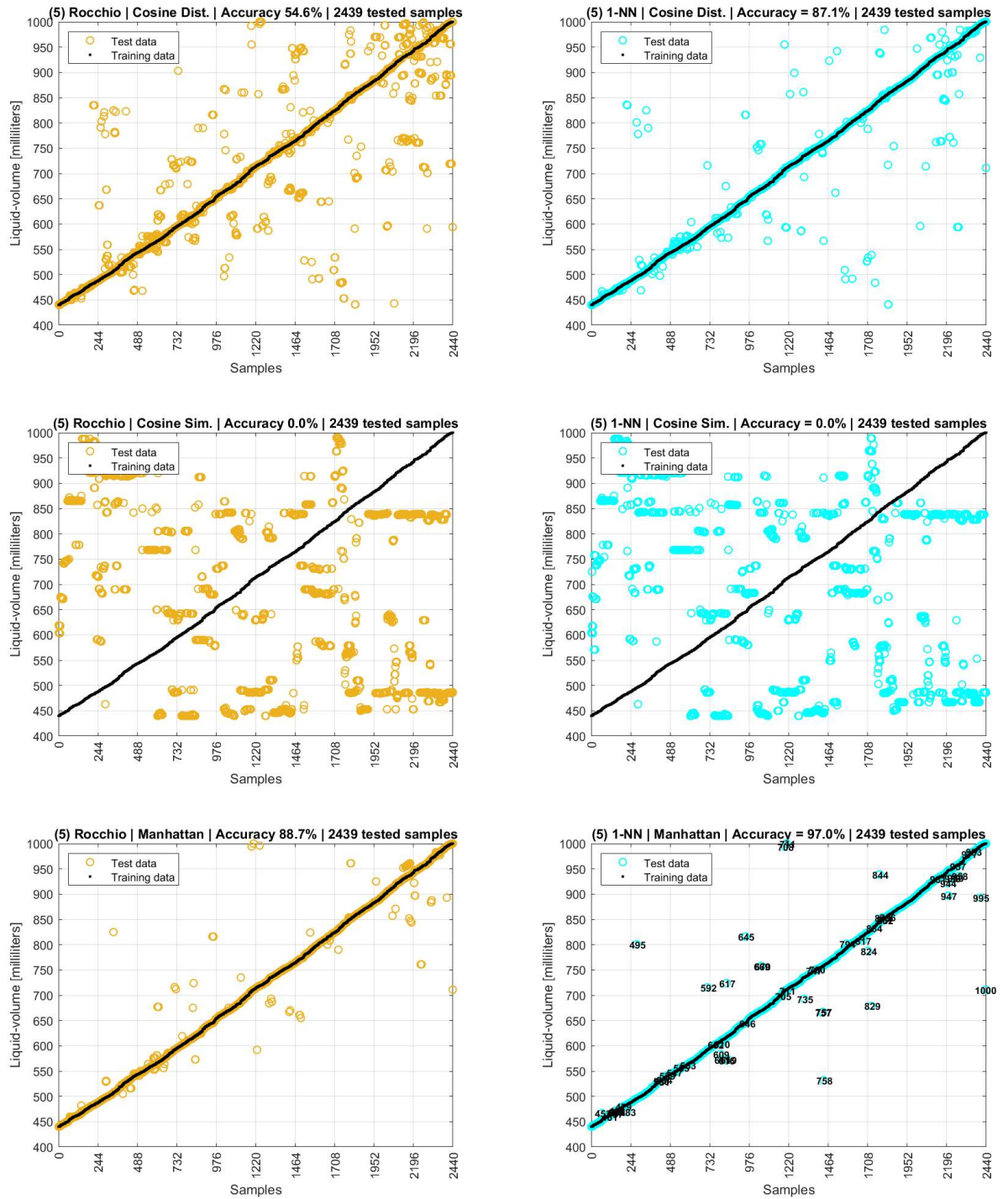
Figure 28. Fifth scenario. This figure has ten graphs distributed in two columns and five lines. Graphs on the left column are of Rocchio and on the right are of 1-NN. Each line stands for a different distance metrics. Each graph title has the name of distance used, the resulting accuracy and number of tested samples.

These distance-based analyses could have been stopped with the fifth scenario, as an accuracy above 95% has been found. However, perceiving the result of Manhattan's distance metrics in the fifth scenario, a sixth and last scenario was purposed with the goal of testing new attribute models and data sources only using that metrics. The data sources differentiate from each other according to the three

actions of phase adjustments previously presented. A phase series can be (i) the original; (ii) the adjusted to −180°/+180°; (iii) the unwrapped; and (iv) the unwrapped with exclusions of deviations above 60°.

After tests, the best accuracy found for the sixth scenario occurred when the data model attributes and data tuples selection were performed the same way of the fifth scenario, but the phases were the original ones collected from the experiment, without any adjustment actions. A fine tuning in the data model was also applied, in which different combinations of the interquartile and percentiles were evaluated using the features of outliers indicators originally registered by the FOH's MA application. As they are four variables, sixteen combinations of two outliers and two measurands were evaluated, and their results are presented in Table 3. When an outlier exclusion is applied, it is shown by an 'x' in the table. Figure 29 shows the best graphic results derived from theses analyses.

Table 3. Sixth scenario results for Rocchio and 1-NN with Manhattan and outlier selections.

Test	Amplitude		Phase			Manhattan	
	Quartile	Percentile	Quartile	Percentile	Samples	Rocchio	1-NN
1	x	x	x	x	1799	96.1%	99.1%
2	x	x	x		2170	**97.3%**	**99.4%**
3	x	x		x	1801	96.3%	98.7%
4	x	x			2226	96.0%	99.3%
5	x		x	x	2120	96.9%	99.1%
6	x		x		2551	96.7%	99.0%
7	x			x	2122	96.3%	99.2%
8	x				2622	95.9%	99.2%
9		x	x	x	1811	96.3%	99.0%
10		x	x		2186	96.1%	98.9%
11		x		x	1814	95.9%	99.0%
12		x			2244	96.1%	98.8%
13			x	x	2240	96.1%	98.8%
14			x		2697	95.9%	98.5%
15				x	2244	95.8%	98.6%
16					2805	92.3%	98.0%
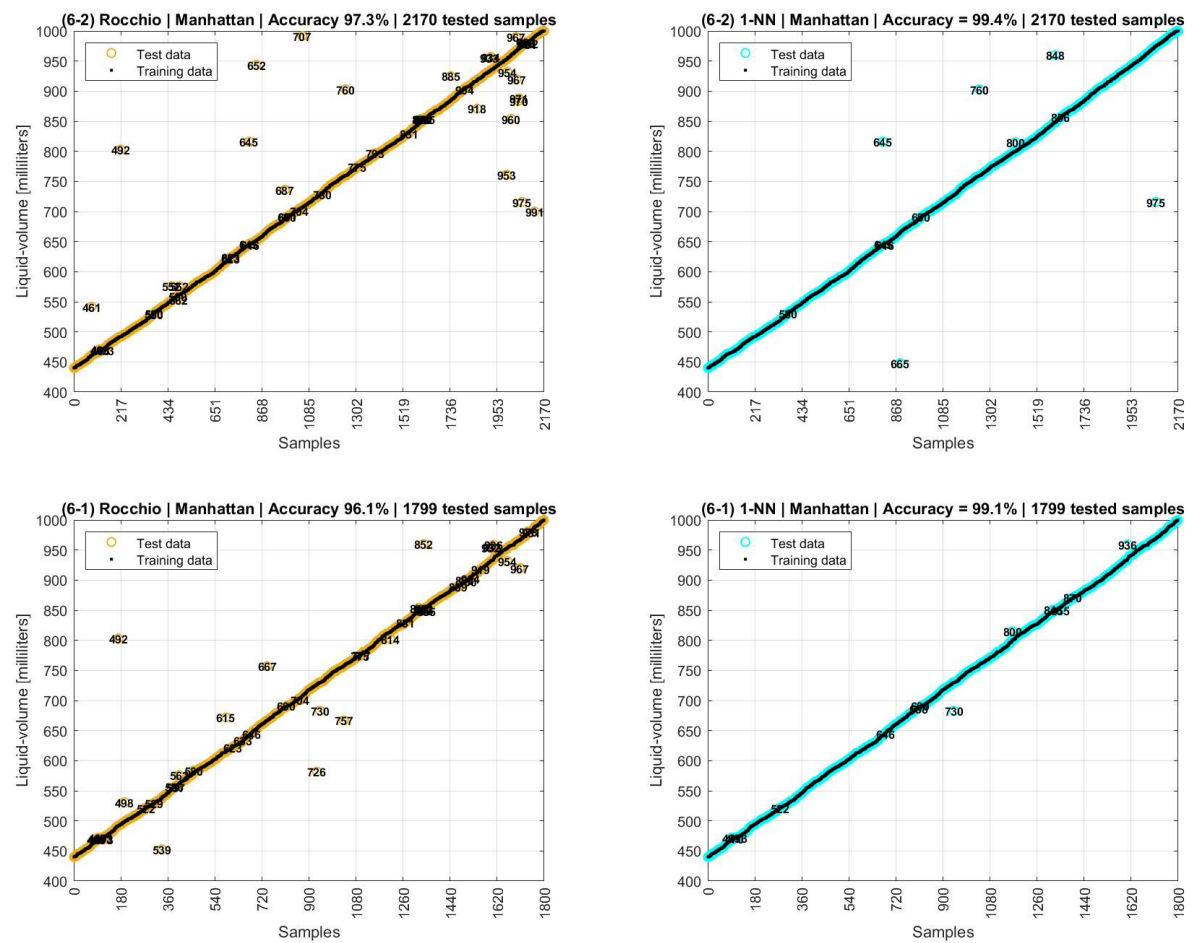
Figure 29. Rocchio and 1-NN accuracies with Manhattan distances over original data collected.

Although Test 2 of Table 3 presented the greatest accuracy of 99.4% among other 16 tests, Figure 29 shows that Test 1 also has a high accuracy of 99.1% but a cleaner graph, in which the distances between the correct and the wrong predicted liquid volumes are shorter. This result shows that the simultaneous application of both outliers exclusion strategies on Test 1, interquartile and percentile, on both amplitude and phase series, it has eliminated more noisy values then did the Test 2. Therefore, although Test 1 (99.1%) has a slightly lower accuracy than Test 2 (99.4%), the Test 1 is preferable as a model, as it has classification errors with smaller deviations around the right liquid-volumes.

The use of distance-based machine learning algorithms was prominent to this work as the results achieved the accuracy of 99.4% for 1-NN and 97.3% for Rocchio, with both using the Manhattan's distance metrics. Values of 3-NN=99.1% and 5-NN=98.5% were calculated, proving that one neighborhood models have better accuracies. The accuracies for Euclidean distance in sixth scenario were 88.5% for Rocchio and 98.0% for 1-NN.

The Manhattan's metrics represents the distance between two points measured along axes at right angles of 90° degrees, following a grid approach instead of the straight-lines of Euclidean's distance

(SINGH, 2019). When comparing a measured and a reference signal, similarity methods based on Manhattan metrics can be used to minimize the distances between those signals (HARTOG, 2016; WANG, F. et al., 2015). Besides the better accuracies, the Manhattan's metrics is preferable then Euclidean in terms of resource consumption, as Euclidean requires squared-root operations, and Manhattan needs only the absolute value of a subtraction (SAINI et al., 2018).

4.8   GAUSSIAN PROCESS REGRESSION

A Gaussian Process Regression (GPR) algorithm was configured with the method of rational quadratic type, and the resulting R2 of 1.00 and the RMSE of 0.21164 are shown in Figure 30. An error of 0.2 over supervised data collected with the steps of 1.0 ml shows a great fit of the GPR over the nature of physics involved in this experiment.

Figure 30. Gaussian process regression (rational quadratic) for the FOH system.
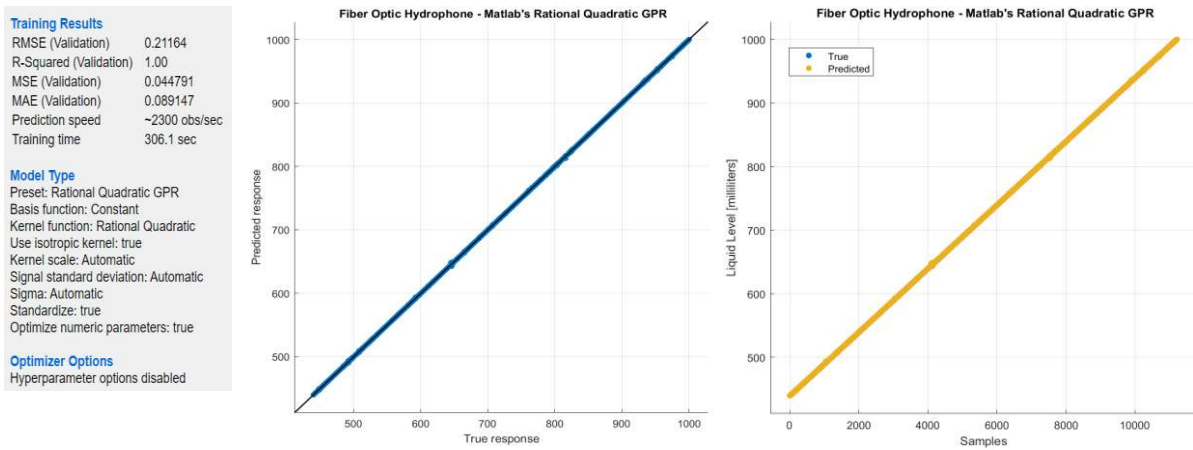
Therefore, ending the results and discussion, different machine learning algorithms have been evaluated, in which two were of classification and one was of regression type. A model fit to the unwrapped phase was also shown. The classification algorithms were assessed considering five different distance metrics.

A summary and results of machine learning scenarios assessed are presented in Table 4.

Table 4. Summary of the six scenarios evaluated using distance-based machine learning algorithms.

Scenar-ios	Phase Series	Training Model / Tested Samples / Features Outliers Exclusions	Distance Metrics	Algorithm Rocchio Accuracy	Algorithm K-NN Accuracy
1	Adjusted by Action(a): −180°/+180°	Only **Mode** Centroids 561 samples / 3 features None	Euclidean	96.8%	31.2% (3-NN)
2	Adjusted by Action(a): −180°/+180°	Only **Mean** Centroids 561 samples / 3 features None	Euclidean	100%	29.8% (3-NN)
3	Adjusted by Action(a): −180°/+180°	**Modes + Means** Centroids 561 samples / 5 features None	Euclidean	100%	31.4% (3-NN)
4	Adjusted by Action(a): −180°/+180°	**Modes + Means** Centroids 9682 samples / 5 features Interquartile	Euclidean	57.8%	25.0% (3-NN) 15.8% (5-NN)
5	Adjusted by the **Three Actions**: Unwrapped	**Complete Dataset** TR|TS = 75%|25% (random) 2439 samples / 12 features None	**Euclidean**	71.4%	**91.6% (1-NN)** 87.9% (3-NN)
			Mahalanobis	74.8%	89.3% (1-NN)
			Cosine Distance	54.6%	87.1% (1-NN)
			Cosine Similarity	0.0%	0.0% (1-NN)
			Manhattan	**88.7%**	**97.0% (1-NN)**
6	**Very Original Data Collected (No adjustments)**	**Complete Dataset** TR|TS = 75%|25% (random) 2170 samples / 12 features Interquartile + Percentiles	**Manhattan**	97.3%	**99.4%**

After all analyses, the best results are presented in Table 5.

Table 5. Results of machine learning algorithms used for the liquid volume predictions.

Machine Learning Algorithms		Distance/Type	Metrics	Value
Classification	**k-NN 1**	**Manhattan**	Accuracy	**99.4%**
	Rocchio	Manhattan		97.3%
	k-NN 1	Euclidean		93.1%
	Rocchio	Euclidean		75.1%
	k-NN 1	Mahalanobis		90.6%
	Rocchio	Mahalanobis		76.1%
	k-NN 1	Cosine Distance		90.9%
	Rocchio	Cosine Distance		64.6%
Regression	Sum of Sines	Nine terms	RMSE%	4.15%
			R^2	0.9994
	Gaussian Process	Rational Quadratic	RMSE	**0.21164 ml**
			R^2	**1.0000**

5 CONCLUSIONS AND FUTURE WORKS

In this work, a fiber-optic hydrophone (FOH) based on the Michelson's interferometer (MI) is actively stabilized by an electronic feedback (EF) loop circuit to mitigate mechanical and thermal noises coming from the external environment. The FOH system is employed as a hardware and software application to perform liquid-volume measurements of a graduated cylinder glass of 1000 ml, filled with water, whose testing volumes ranged from 440 ml to 1000 ml. This range limitation is due to setup arrangements and positioning of the ultrasound source inside the cylinder. The sensing elements are composed by two optical fiber coils placed at the sensor head and a third optical fiber coil is placed at the MI's reference arm. The coils are made with readily available and common SMF fiber. The reference coil is wound around a piezoelectric actuator to stabilize the system at the quadrature point of $\pi/2$, and the two sensor coils are submerged into water to detect acoustic wave oscillations related to liquid volume variations, supplying distinct values of amplitudes (volts) and phases (degrees) as output measurands. Finally, due to the non-linear behavior of theses measurands, machine learning algorithms have been employed under supervised learning to predict the liquid-volumes.

5.1 CONTRIBUTIONS

The main contribution of this work is the accuracy of 99.4% achieved what is a prominent result in liquid volume predictions for a system that employs acoustics detection through optical fiber sensors. Also, an RMSE of 0.21164 ml shows the feasibility of the FOH system. For the test tank used, the value of 0.21164 ml is equivalent to 0.0714 mm of error in the height of the water. Other result was the characterization of the unwrapped phase measurand, in which a sum of sines fitting function reached an R2 of 0.9994 and an RMSE% of 4.15%.

Other contribution from this work is a practical demonstration of the homodyne demodulation approach working with an active stabilization mechanism over a Michelson's interferometer, as (KIRKENDALL; DANDRIDGE, 2004) mentions that it is a challenge to stabilize such system for sensing applications, and it is useful for laboratory analysis. The advantages and drawbacks of quadrature stabilization methods are related to the resolution of the interferometer, which is the smallest physical quantity that a sensor can measure, defined by the noise of the measurand. Multiple reflections in optical arms improve the resolution of a homodyne interferometer but can induce phase jumps and loss of laser coherence. Therefore, a compromise must be found between the increase in resolution and the loss of coherence (WATCHI et al., 2018).

5.2 LIMITATIONS

As a limitation, this first version of the FOH system was used to measured only one type of liquid (water), although the two optical coils in MI's sensor head were intentionally constructed to find different fluids around them (e.g., water and oil), what will be done in future tests. Other limitation is the medium time of 3 (three) seconds to collect and process one data sample. As a milliliter requires twenty samples, the FOH system lasts a minute to predict a liquid volume.

5.3 PUBLICATION

This work resulted in the following paper publication:

- Duque, W.S.; Rodríguez Díaz, C.A.; Leal-Junior, A.G.; Frizera, A. Fiber-Optic Hydrophone Based on Michelson's Interferometer with Active Stabilization for Liquid Volume Measurement. Sensors 2022, 22, 4404. https://doi.org/10.3390/s22124404.

5.4 FUTURE WORKS

As suggestions for future works, this system can be improved to detect different fluids and multifluid interfaces. It might be worth it to also verify the results after some little hardware arrangements, as taking out the polarization controllers, in order to look for opportunities of optimizing the system's components. Second, the stabilized FOH can also be used, with few adaptations, to perform ultrasound piezo-electric transducer calibrations (CHANG; ZHU; YANG, 2015; PRESTON et al., 1999). Third, the FBG structure proposed by (DÍAZ, Camilo Arturo Rodríguez et al., 2018; LEAL-JUNIOR et al., 2019) could include an optical coil inside or wound around the polymer diaphragm structure as an additional sensor to read information about mechanic vibration patterns of fluids in production vessels. Finally, a LSTM (Long short-term memory) could be used as a prediction model as the recursive behavior of that neural network would be capable of detecting a sequence of points in the 'snail paths' shown in the two-dimensional plane of modal amplitude and phase patterns previously demonstrated in Figure 23.

References

AL-NAAMANY, A. M.; MERIBOUT, M.; AL BUSAIDI, K. Design and implementation of a new nonradioactive-based machine for detecting oil-water interfaces in oil tanks. **IEEE Transactions on Instrumentation and Measurement**, v. 56, n. 5, p. 1532–1536, out. 2007.

ALBALATE, A.; MINKER, W. **Semi-Supervised and Unsupervised Machine Learning**. [S.l.]: John Wiley and Sons, 2011.

BEARD, P. C.; HURRELL, A. M.; MILLS, T. N. Characterization of a polymer film optical fiber hydrophone for use in the range 1 to 20 MHz: a comparison with PVDF needle and membrane hydrophones. **IEEE Transactions on Ultrasonics, Ferroelectrics, and Frequency Control**, 2000.

BELL, A. G. Upon the production and reproduction of sound by light. **American Association for the Advancement of Sciences**, p. 404–426, 1880.

BUCARO, J. A.; DARDY, H. D.; CAROME, E. F. Fiber-optic hydrophone. **Journal of the Acoustical Society of America**, v. 62, n. 5, p. 1302–1304, 1977a.

_____. Optical fiber acoustic sensor. **Applied Optics, Vol. 16, Issue 7, pp. 1761-1762**, v. 16, n. 7, p. 1761–1762, 1 jul. 1977b. Disponível em: <https://opg.optica.org/viewmedia.cfm?uri=ao-16-7-1761&seq=0&html=true>. Acesso em: 8 mar. 2022.

BUCARO, J. A.; HICKMAN, T. R. Measurement of sensitity of optical fibers for acoustic detection. **Applied Optics, Vol. 18, Issue 6, pp. 938-940**, v. 18, n. 6, p. 938–940, 15 mar. 1979. Disponível em: <https://opg.optica.org/viewmedia.cfm?uri=ao-18-6-938&seq=0&html=true>. Acesso em: 28 maio 2022.

BUICK, J. M. et al. Application of the acousto-optic effect to pressure measurements in ultrasound fields in water using a laser vibrometer. **Review of Scientific Instruments**, v. 75, n. 10 I, p. 3203–3207, 2004.

CAMPANELLA, C. E. et al. Fibre Bragg Grating based strain sensors: review of technology and applications. **Sensors (Switzerland)**, v. 18, n. 9, 2018.

CEJA, E. G. **Behavior analysis with machine learning using R**. [S.l.]: CRC Press, 2022. Disponível em: <https://www.researchgate.net/publication/269107473_What_is_governance/link/548173090cf22525dcb61443/download%0Ahttp://www.econ.upf.edu/~reynal/Civil wars_12December2010.pdf%0Ahttps://think-asia.org/handle/11540/8282%0Ahttps://www.jstor.org/stable/41857625>.

CHAN, H. L. W. et al. Use of a fibre-optic hydrophone in measuring acoustic parameters of high power hyperthermia transducers. **Physics in Medicine and Biology**, v. 34, n. 11, p. 1609–1622, nov. 1989. Disponível em: <http://www.ncbi.nlm.nih.gov/pubmed/2587628>. Acesso em: 12 mar. 2020.

CHANG, S.; ZHU, H.; YANG, P. An Active Stabilization Technique Of A Homodyne Interferometer Based On PTDC For High Frequency Hydrophone Calibration. **Proceedings of the 3rd International Conference on Mechanical Engineering and Intelligent Systems (ICMEIS 2015)**, v. 26, n. Icmeis, p. 317–324, 2015.

COLE, J. H.; JOHNSON, R. L.; BHUTA, P. G. Fiber-optic detection of sound. **Journal of the Acoustical Society of America**, v. 62, n. 5, p. 1136–1138, 1977.

COLE, James H. et al. The origin, history and future of fiber-optic interferometric acoustic sensors for US Navy applications. **21st International Conference on Optical Fiber Sensors**, v. 7753, p. 775303, 15 maio 2011.

CULSHAW, B. Optical fibre sensors: a compressed perspective. 21 dez. 2017, [S.l.]: Institute of Electrical and Electronics Engineers Inc., 21 dez. 2017. p. 1–3.

DA SILVA MARQUES, R. et al. Corrosion resistant FBG-based quasi-distributed sensor for crude oil tank

dynamic temperature profile monitoring. **Sensors (Switzerland)**, v. 15, n. 12, p. 693–703, 2015.

DAVIS, A. R. et al. 64 Channel All Optical Deployable Acoustic Array. v. 16, p. OFA6, 6 jan. 2015.

DE PAULA, R. P.; COLE, J. H.; BUCARO, J. A. Broad-Band Ultrasonic Sensor Based on Induced Optical Phase Shifts in Single-Mode Fibers. **Journal of Lightwave Technology**, v. 1, n. 2, p. 390–393, 1983.

DÍAZ, Camilo A. R. et al. Perrogator: a portable energy-efficient interrogator for dynamic monitoring of wavelength-based. **Sensors**, v. 19, n. 2962, p. 18, 2019. Disponível em: <www.mdpi.com/journal/sensors>.

DÍAZ, Camilo Arturo Rodríguez et al. Liquid level measurement based on FBG-embedded diaphragms with temperature compensation. **IEEE Sensors Journal**, v. 18, n. 1, p. 193–200, 2018.

_____. Optical Fiber Sensing for Sub-Millimeter Liquid-Level Monitoring: A Review. **IEEE Sensors Journal**, v. 19, n. 17, 2019. Disponível em: <https://ieeexplore-ieee-org.ez43.periodicos.capes.gov.br/document/8706966/>. Acesso em: 2 dez. 2021.

ELEZOV, M. S. et al. Active and passive phase stabilization for the all-fiber Michelson interferometer. **Journal of Physics: Conference Series**, v. 1124, n. 5, 2018.

FAISAL, S.; BUKHARI, A.; YANG, W. Multi-interface Level Sensors and New Development in Monitoring and Control of Oil Separators. **Sensors 2006, Vol. 6, Pages 380-389**, v. 6, n. 4, p. 380–389, 7 abr. 2006. Disponível em: <https://www.mdpi.com/1424-8220/6/4/380/htm>. Acesso em: 6 abr. 2022.

FAN, H. et al. Ultracompact twisted silica taper for 20 kHz to 94 MHz ultrasound sensing. **Optics Letters**, v. 45, n. 14, p. 3889, 2020.

_____. Ultrasound sensing based on an in-fiber dual-cavity Fabry–Perot interferometer. **Optics Letters**, v. 44, n. 15, p. 3606–3609, 1 ago. 2019. Disponível em: <https://opg.optica.org/viewmedia.cfm?uri=ol-44-15-3606&seq=0&html=true>. Acesso em: 25 maio 2022.

FAN, H.; CHEN, L.; BAO, X. Chalcogenide microfiber-assisted silica microfiber for ultrasound detection. **Optics Letters**, v. 45, n. 5, p. 1128, 2020.

FORESTIERI, E. et al. High-Speed Optical Communications Systems for Future WDM Centralized Radio Access Networks. **Journal of Lightwave Technology**, v. 8724, n. c, p. 1–1, 2021. Disponível em: <https://ieeexplore.ieee.org/document/9629243/>. Acesso em: 8 dez. 2021.

GRASSANI, D.; GALLI, M.; BAJONI, D. Active stabilization of a Michelson interferometer at an arbitrary phase with subnanometer resolution. **Optics Letters**, v. 39, n. 8, p. 2530, 2014.

HARTOG, A. H. **An introduction to distributed optical fibre sensors**. Boca Raton, FL: CRC Press - Taylor & Francis Group, LLC, 2016.

HJERTAKER, B. T. Level measurement and control strategies for subsea separators. **Journal of Electronic Imaging**, 2001.

HJERTAKER, B. T.; JOHANSEN, G. A.; JACKSON, P. Recent developments in hydrocarbon separator interface imaging. 2001, [S.l: s.n.], 2001.

HU, J.; LI, D. Simulation and testing of a noise-limited demodulation system for a fiber-optic hydrophone system based on a Michelson interferometer. **2016 IEEE/OES China Ocean Acoustics Symposium, COA 2016**, 5 ago. 2016.

HU, J.; LI, D.; LIU, H. Research on noise floor of an interferometric fiber-optic hydrophone system. **2017 IEEE International Conference on Signal Processing, Communications and Computing, ICSPCC 2017**, v. 2017- Janua, p. 1–4, 29 dez. 2017.

JAMES, G. et al. **An Introduction to Statistical Learning with Applications in R**. Second Edi ed. [S.l.]: Springer, 2021.

JARZYNSKI, J.; HUGHES, R. Static pressure sensitivity amplification in interferometric fiber-optic hydrophones. **Applied Optics, Vol. 19, Issue 1, pp. 98-107**, v. 19, n. 1, p. 98–107, 1 jan. 1980. Disponível em: <https://opg.optica.org/viewmedia.cfm?uri=ao-19-1-98&seq=0&html=true>. Acesso em: 28 maio 2022.

KATTI FACELI, ANA CAROLINA LORENA, JOÃO GAMA, A. C. P. L. F. de C. **Inteligência artificial: uma abordagem de máquina**. Rio de Janeiro: LTC, 2011.

KIMURA, K.; TAKEUCHI, S.; KOIKE, Y. Investigation of Cavitation Bubble Influence on Frequency Spectrum of Fiber Optic Probe Hydrophone Output. 2020, [S.l.]: IEEE, 2020. Disponível em: <https://ieeexplore-ieee-org.ez43.periodicos.capes.gov.br/document/9251534/>. Acesso em: 20 fev. 2022.

KIRKENDALL, C. K.; DANDRIDGE, A. Overview of high performance fibre-optic sensing. **Journal of Physics D: Applied Physics**, v. 37, n. 18, 21 set. 2004.

KROHN, D.; MACDOUGALL, T.; MENDEZ, A. **Fiber Optic Sensors: fundamentals and applications**. Fourth edi ed. Bellingham, Washington, USA: Society of Photo-Optical Instrumentation Engineers (SPIE) All, 2014.

LEAL-JUNIOR, A. G. et al. Multi-interface level in oil tanks and applications of optical fiber sensors. **Optical Fiber Technology**, v. 40, p. 82–92, 2018. Disponível em: <https://doi.org/10.1016/j.yofte.2017.11.006>.

_____. Simultaneous measurement of pressure and temperature with a single FBG embedded in a polymer diaphragm. **Optics and Laser Technology**, v. 112, 2019.

LEE, B. H. et al. Interferometric Fiber Optic Sensors. **Sensors 2012, Vol. 12, Pages 2467-2486**, v. 12, n. 3, p. 2467–2486, 23 fev. 2012. Disponível em: <https://www.mdpi.com/1424-8220/12/3/2467/htm>. Acesso em: 2 dez. 2021.

LIANG, X. et al. In-fiber liquid-level probe based on Michelson interferometer via dual-mode elliptical multilayer-core fiber. **Journal of Modern Optics**, v. 63, n. 13, p. 1254–1259, 19 jul. 2016. Disponível em: <https://www.researchgate.net/publication/291558336_In-fiber_liquid-level_probe_based_on_Michelson_interferometer_via_dual-mode_elliptical_multilayer-core_fiber>. Acesso em: 2 dez. 2021.

LUBBERS, J.; GRAAFF, R. A simple and accurate formula for the sound velocity in water. **Ultrasound in Medicine and Biology**, v. 24, n. 7, p. 1065–1068, 1 set. 1998.

MA, J. et al. Low cost, high performance white-light fiber-optic hydrophone system with a trackable working point. **Optics Express**, v. 24, n. 17, p. 19008, 2016.

MANNING, C. D.; RAGHAVAN, P.; SCHUTZE, H. **Introduction to Information Retrieval**. [S.l.]: Cambridge University Press, 2008.

MASSEY, G. A. An Optical Heterodyne Ultrasonic Image Converter. **Proceedings of the IEEE**, v. 56, n. 12, p. 2157–2161, 1968.

MENG, Z. et al. Recent Progress in Fiber-Optic Hydrophones. **Photonic Sensors**, v. 11, n. 1, p. 109–122, 1 mar. 2021. Disponível em: <https://go.gale.com/ps/i.do?p=AONE&sw=w&issn=21907439&v=2.1&it=r&id=GALE%7CA651496455&sid=googleScholar&linkaccess=fulltext>. Acesso em: 8 dez. 2021.

MERIBOUT, M.; NAAMANY, A. Al; BUSAIDI, K. Al. An acoustic system for providing the two-phase liquid profile in oil field storage tanks. **IEEE Transactions on Ultrasonics, Ferroelectrics, and Frequency Control**,

v. 56, n. 10, p. 2241–2250, 2009.

MITCHELL, T. M. **Machine learning**. New York: McGraw-Hill, 1997.

MONSAY, E. H.; GILBERT, D. E. Predicted performance of a heterodyne detector with a fiber optic coil hydrophone. **Oceans Conference Record (IEEE)**, v. 1, p. 31–34, 1981.

MORRIS, P. et al. A fabry-perot fibre-optic hydrophone for the measurement of ultrasound induced temperature changes. **Proceedings - IEEE Ultrasonics Symposium**, v. 1, n. November, p. 536–539, 2006.

MORRIS, P.; BEARD, P.; HURRELL, A. Development of a 50MHz optical fibre hydrophone for the characterisation of medical ultrasound fields. 2005, [S.l: s.n.], 2005.

MOSS, G. E.; MILLER, L. R.; FORWARD, R. L. Photon-Noise-Limited Laser Transducer for Gravitational Antenna. **Applied Optics**, v. 10, n. 11, p. 2495, 1 nov. 1971.

PRESTON, R. C. et al. Primary calibration of membrane hydrophones in the frequency range 0.5 MHz to 60 MHz. **Metrologia**, 1999.

REIDER, G. A. **Photonics: An Introduction**. Vienna, Austria: Springer International Publishing Switzerland, 2016.

ROGERS, S.; GIROLAMI, M. **A first course in machine learning**. 2. ed. Boca Raton, FL: CRC Press - Taylor & Francis Group, LLC, 2017.

RUPITSCH, S. J. **Piezoelectric sensors and actuators: fundamentals and applications**. [S.l.]: Springer, 1992.

_____. **Piezoelectric Sensors and Actuators: Fundamentals and Applications**. [S.l: s.n.], 2019.

RUSSEL, S. J.; NOVIG, P. **Artificial intelligence: a modern approach**. Fourth Edi ed. [S.l.]: Pearson, 2022. Disponível em: <www.pearsonglobaleditions.com>.

SAINI, H. S. et al. **Innovations in Electronics and Communication Engineering**. Warsaw, Poland: Springer, 2018. v. 65. Disponível em: <http://link.springer.com/10.1007/978-981-10-8204-7>.

SATTAR, F. et al. A new event detection method for noisy hydrophone data. **Applied Acoustics**, v. 159, 1 fev. 2020.

SHAO, L. Y. et al. High-frequency ultrasonic hydrophone based on a cladding-etched DBR fiber laser. **IEEE Photonics Technology Letters**, v. 20, n. 8, p. 548–550, 2008.

SHEN, B. et al. Fiber-optic ultrasonic probe based on refractive-index modulation in water. **21st International Conference on Optical Fiber Sensors**, v. 7753, p. 77539W, 2011.

SINGH, H. **Practical Machine Learning and Image Processing**. [S.l: s.n.], 2019. Disponível em: <https://doi.org/10.1007/978-1-4842-4149-3>.

STAUDENRAUS, J.; EISENMENGER, W. Fibre-optic probe hydrophone for ultrasonic and shock-wave measurements in water. **Ultrasonics**, v. 31, n. 4, p. 267–273, 1993.

THE MATH WORKS INC. **MATLAB. Version 9.11.0.1873467 (R2021b) Update 3 (Student License)**. . Natick, Massachusetts: The Mathworks, Inc. , 2021

UDD, E.; WILLIAM B. SPILLMAN, J. **Fiber Optic Sensors: An Introduction for Engineers and Scientists**. 2nd. ed. [S.l.]: Wiley, 2011.

VORATHIN, E. et al. **Review of high sensitivity fibre-optic pressure sensors for low pressure sensing**.

Optics and Laser Technology. [S.l.]: Elsevier Ltd. , 1 jan. 2020

WANG, C. C. et al. Very high responsivity fiber optic hydrophones for commercial applications. **SPIE**, v. 2360, p. 360–363, 14 set. 1994. Disponível em: <https://ui.adsabs.harvard.edu/abs/1994SPIE.2360..360W/abstract>. Acesso em: 28 maio 2022.

WANG, F. et al. Determining the Change of Brillouin Frequency Shift by Using the Similarity Matching Method. **Journal of Lightwave Technology**, v. 33, n. 19, 2015. Disponível em: <https://ieeexplore-ieee-org.ez43.periodicos.capes.gov.br/document/7214198/>. Acesso em: 19 abr. 2022.

WANG, L. et al. The arctangent approach of digital PGC demodulation for optic interferometric sensors. **Interferometry XIII: Techniques and Analysis**, v. 6292, p. 62921E, 14 ago. 2006.

WANG, M. et al. Measurement of underwater acoustic pressures in the frequency range 25 to 500 kHz using optical interferometry and discussion on associated uncertainties. **25th International Congress on Sound and Vibration 2018, ICSV 2018: Hiroshima Calling**, v. 8, n. July, p. 4909–4914, 2018.

WANG, W. et al. High-Sensitivity Cuboid Interferometric Fiber-Optic Hydrophone Based on Planar Rectangular Film Sensing. **Sensors 2020, Vol. 20, Page 6422**, v. 20, n. 22, p. 6422, 10 nov. 2020. Disponível em: <https://www.mdpi.com/1424-8220/20/22/6422/htm>. Acesso em: 5 abr. 2022.

WATCHI, J. et al. Contributed Review: A review of compact interferometers. **Review of Scientific Instruments**, v. 89, n. 12, p. 121501, 21 dez. 2018. Disponível em: <https://aip.scitation.org/doi/abs/10.1063/1.5052042>. Acesso em: 11 mar. 2022.

WILD, G.; HINCKLEY, S. Acousto-ultrasonic optical fiber sensors: Overview and state-of-the-art. **IEEE Sensors Journal**, v. 8, n. 7, p. 1184–1193, jul. 2008.

WURSTER, C.; STAUDENRAUS, J.; EISENMENGER, W. The fiber optic probe hydrophone. **Proceedings of the IEEE Ultrasonics Symposium**, v. 2, p. 941–944, 1994.

XIE, F.; CHEN, Z.; REN, J. Stabilisation of an optical fiber Michelson interferometer measurement system using a simple feedback circuit. **Measurement: Journal of the International Measurement Confederation**, v. 42, n. 9, p. 1335–1340, 2009. Disponível em: <http://dx.doi.org/10.1016/j.measurement.2009.04.009>.

XU, R. U. I. et al. **Clustering**. [S.l.]: John Wiley & Sons, Inc., 2009.

YANG, F. et al. Miniature interrogator for multiplexed FBG strain sensors based on a thermally tunable microring resonator array. **Optics Express**, v. 27, n. 5, p. 6037–6046, 2019.

YANG, Y. et al. High-Performance Fiber Optic Interferometric Hydrophone Based on Push-Pull Structure. **IEEE Transactions on Instrumentation and Measurement**, v. 70, 2021.

YIN, S.; RUFFIN, P. B.; YU, F. T. S. **Fiber Optic Sensors**. 2nd. ed. Boca Raton, FL: CRC Press - Taylor & Francis Group, LLC, 2008.